GDRI GEOMECH

Multi-Physics and Multiscale Couplings in Geo-environmental Mechanics

Annual Seminar

La Rochelle, 11-13 June 2018

Book of extended abstracts

Edited by Pierre-Yves Hicher and Pearl-Angelika Lee

Preface

The GDRI GeoMech international network was created in January 2016, as a follow-up of the French network GDR MeGe. During 8 years, GDR MeGe gathered the main French groups involved in the broad field of geomechanics, with a special focus on environmental applications. Taking advantage of the collaborations and connections that the partners had developed with foreign universities, extending the network in an international perspective was a natural ambition. The goal of GDRI GeoMech is thus to further promote the French community involved in geomechanics and to strengthen its national and international positioning and visibility.

Today, GDRI GeoMech brings together more than 25 partners from many countries, including the Netherlands, Italy, Spain, Canada, USA and China, with the aim of structuring the existing community working on Multi-physics and Multiscale Couplings in Geo-environmental Mechanics. Its main lines of research are:

- Catastrophic failures and triggering mechanisms
- Safety of storage reservoirs
- Energy geomechanics.

GDRI GeoMech serves as a common platform for spreading and sharing recent research outcomes, extending international collaborations as well as organizing international scientific meetings and other related events.

This booklet gathers the extended abstracts of the oral presentations given during the annual seminar held in La Rochelle (11-13 June 2018).

With nearly 40 attendees, and nearly 30 oral presentations giving rise to extremely stimulating discussions, there is no doubt that this seminar was a real success, shedding light on the last advances within the GDRI community.

This Proceeding would have never been possible without Angelika and Pierre-Yves Hicher, who have collected and revised all the abstracts. We would like to gratefully acknowledge them for their very much appreciated contribution!

Olivier Millet & François Nicot
Directors of GDRI GeoMech

Artificial Intelligence: a new paradigm of knowledge

Félix Darve, Emeritus Professor

Grenoble Alpes University, Grenoble INP, 3SR Laboratory
Felix.darve@3sr-grenoble.fr

After decades of experimental probing, artificial intelligence has emerged today as a force to be reckoned with not only on a scientific level but also in different fields of human activity.
We will see, after a brief recall of the definition of artificial intelligence, why this eruption could lead to a major revolution in the history of humanity and we will conclude by giving some examples of its current application in engineering sciences.

1. **What is Artificial Intelligence?**

Artificial intelligence is basically the construction of an artificial neuronal network and the implementation of a learning process from the given fact of a certain number of known solutions.
The initial idea of an artificial neuron is based on the reproduction of the biological neuron in the brain of living beings, schematically constituted by thousands of dendrites converging upon a nucleus out of which a single axon emerges (Fig.1).

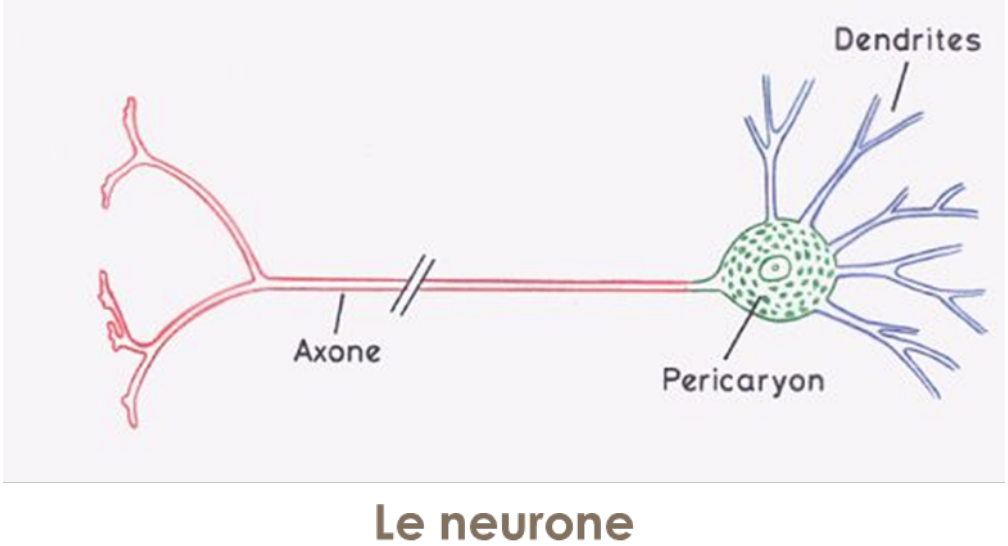

Fig.1: schematic representation of a biological neuron of a living being

Several billions of neurons, interconnected through synapses, are present in our brain. The stimuli are transmitted by electrical micro-impulsions coupled with chemical processes.
An artificial neuronal network is thus constituted by the nodes, disposed in layers and interconnected through links.

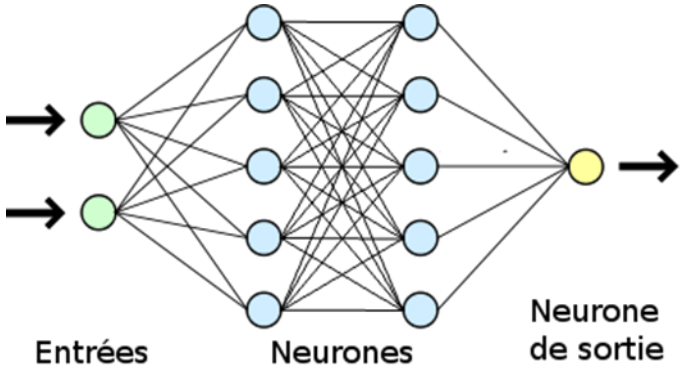

Fig.2: artificial neuronal network

At the origin of the development of artificial intelligence, the neuronal network was constituted by some dozens of nodes situated in several layers disposed on a plane. This method could have been considered as a simple method of interpolation between known data by their users. Today, the "massic" neuronal networks consist of millions of nodes distributed in 3D and their creative extrapolation capacities has been established [1]. For example, in the game of GO, strategies unknown to man have already emerged.

As far as the learning process of a neuronal network is concerned, it is necessary to introduce from the outset (see Fig.2) data for which the solutions at the outcome are known. The calibration of the network thus comes down to giving to different links the weights determined through the learning process by the mathematical methods of retro-gradients.
This calibration ends up in an implicit definition of the hyper-surface passing through a set of points, of which the coordinates correspond to entries and exits. This hyper-surface then provides for the new data a unique determined exit if the surface is sufficiently regular [2]. Although, in these applications, the method has encountered quite overwhelming and mainly unexpected success, the mathematical mastering is still far behind.

2. Why Artificial Intelligence represents such a profound revolution?

Until the 1960's, the methodology applied to solve a "well-posed" problem consisted of formulations by a system of mathematical equations. Then, this system developed analytical methods to come up with a solution, specified by another form of analytical expressions consisting of variables or unknown sought functions. It soon became apparent that very few problems could be specifically solved in this manner. As a matter of fact, only certain fields in linear physics were implicated.
The numerical revolution which has become so important in engineering sciences from the end of the 1960's onward, has permitted extending in a remarkable manner the scale of the problems treated. Indeed, practically all the problems which can be formalized today by a system of equation can be solved numerically (on the condition, obviously, that solutions can indeed be determined), even if the presence of bifurcation points could pose formidable numerical difficulties in the convergence of algorithms.
But, with artificial intelligence, a problem can be simply characterised by a complete discrete set of data with their associated responses; this set can then be constituted by millions of data ("big data"). Formalising entries and exits can then be realised by the code itself which can then "learn" without human intervention.
For example, once the rules of a game are introduced, the artificial intelligence code will carry out its own learning process (i.e. it will calibrate itself by determining the weights affected to

the links) by playing against itself. Or, in the case of a driver's license code formulation, the artificial intelligence software can "learn" to drive a car by conducting virtual driving in a situation of virtual reality.

If indeed the artificial neuronal network has attempted to reproduce our network of biological neurons, the learning process of the network has also adopted our manner of solving the problems we confront, not only generally by solving a system of equations, but also by exploiting the accumulated knowledge coming from our home and school education. Similarly, all car drivers had first to assimilate the driver's license code, then go through a certain number of hours of actual driving before being sufficiently "educated" to go on the road, that's to say to have the capacity to steer a car by respecting to the letter the rules of the driver's license code in all circumstances.

Should an accident occur (for example, in the case of a young driver), the learning process may be judged insufficient and further sessions at the driving school may be deemed necessary. Similarly, given artificial intelligence software, if the number of data with solutions is too limited, the hyper-surface evoked in paragraph 1 will be too imprecise for it to respond correctly to the questions which implicate the new data.

3. What are the applications of artificial intelligence for engineering sciences?

The autonomous car, medical diagnosis, DNA analysis, vocal and visual recognition, automatic translation* to cite but these few operations are already examples of artificial intelligence applied to our daily lives.
As for specific examples in civil engineering, we could cite the two major fields of applications currently under way: intelligent robotics and the intelligent exploitation of a high number of data.

* Translator's note: the present text is not a product of artificial intelligence.

Thus, building sites and public work constructions have much to gain through the automation of certain particularly onerous and life-threatening tasks (taking down nuclear facilities, asbestos removal, etc.) or through the intelligent piloting of certain machines in public work projects (bulldozers, etc.)
Moreover, the metrological revolution has permitted the emergence of new families of captors that are less costly, more time-resistant, and low-energy consumptive which can be disposed in high numbers over the fields to be surveyed (landslides, unstable rock-slopes, …) or in the construction works whose behaviour must be controllable (dams, dykes, nuclear installations, large civil engineering structures). A very large data-base can be obtained from temporal and spatial series.
It will become highly interesting and profitable to exploit these data-bases for developing intelligence techniques which will allow critical points to be detected, the mechanisms of potential failure to be analysed, and even new protection regulations to be recommended.

Naturally, these algorithms of artificial intelligence encounter their limits; for example, when the hyper-surface, evoked in paragraph 1, is not sufficiently regular which will lead to the inexistence of solutions or to multiple solutions (bifurcation points of various types) or because the system studied is pathologically sensitive to initial conditions (meteorology, …)
Let us remember that, basically, artificial intelligence is essentially different from biological intelligence in that it lacks consciousness.

Certain researchers, however, consider that just as consciousness appears "spontaneously" in a baby at a certain level of neuronal complexity, a form of consciousness could appear in robots invested with artificial intelligence. In terms of anticipation, a mathematician has even been able to evoke the identical reproduction of a biological neuronal network in the brain of a human being [3] through a neuronal network that is artificial.

References

[1] Google Brain Team, open source software « TensorFlow »
[2] Mallat S., course « Sciences des Données », Collège de France, 2018
[3] Connes A., Chéreau D., Dixmier J., « Le Théatre quantique », *Editions Odile Jacob*, 2013

Shear of a Dilatant Patch at a Pre-compressed Geological Fault

A.P.S. Selvadurai
Department of Civil Engineering and Applied Mechanics, McGill University, Montréal, QC, Canada H3A 0C3
[E-mail: patrick.selvadurai@mcgill.ca;
Web page: http://www.mcgill.ca/civil/people/selvadurai]
P.A. Selvadurai
Schweizerischer Erdbebendienst, Department of Earth Sciences, ETH, 8092 Zürich, Switzerland
A.P. Suvorov
Department of Applied Mathematics, Moscow State University of Civil Engineering (MGSU), Moscow, Russia

Abstract
The paper discusses an approach for examining the shear rupture behaviour of a dilatant region with a circular planform located at a pre-compressed geological interface. The modelling accounts for the unilateral contact at the interface that allows the development of interface separation during dilatant deformations. The role of deterioration of the dilatancy angle with increasing shear displacement is also accommodated and the rupture stress is estimated using the approach proposed by D.W. Taylor (1948) to estimate failure of the dilatant regions. The analysis illustrates how the rupture stress can be influenced by parameters such as the pre-compressive stress, the elastic deformability characteristics of the zones composing the dilatant region, the friction and dilatancy angles and parameters that can describe the degradation of the dilatancy angle with relative shear.

Introduction

The mechanical behaviour of geologic interfaces, particularly faults and fractures, is important to several branches of engineering geosciences including stability of geologic strata, development of tectonic motion, displacements of pre-existing fractures and interaction processes in constructed underground facilities, where the interface behaviour is controlled by the stress state and the influence of both cohesive and frictional forces. The literature in this area is vast (nearly six thousand references covering the diverse areas of geomaterial interfaces, geologic fault zones, tribology, wear, biomechanics, contact mechanics, etc.) and no attempt will be made to provide a complete review of the subject. The reader is referred to the volumes and articles by Desai and Christian (1977), Selvadurai and Boulon (1995), Nguyen and Selvadurai (1998) and Selvadurai and Yu (2005) for further references on these topics. In a majority of classical studies in this area, the focus is on fracture surfaces that exhibit Coulomb friction and consideration of dilatancy and its degradation are relatively rare.

Analysis

In this study, we examine a specific contact problem that illustrates the influence of elastic restraint at a dilatant region and the deterioration of the dilatancy angle with relative shear on the shear rupture of the region. We specifically consider the problem of a dilatant circular patch of radius a that is contained at the interface of two isotropic elastic geologic media with elastic constants (G,ν) and under the action of a pre-compression stress σ_0. The region exterior to the dilatant circular patch is assumed to be frictionless. The two halfspace regions are subjected to a lateral relative shear displacement $2\Delta u$ and during this shear deformation, the dilatancy processes can induce a displacement $2\Delta v$ in the circular patch, which in turn can induce separation at the pre-compressed interface (Figure 1).

The resulting unilateral contact problem is three-dimensional and can only be solved by appeal to computational approaches. In this study, however, we assume that the contact problem can be approximated by axisymmetric states of deformation. This enables us to study the unilateral contact problem in order to estimate the radius of the zone of separation at the interface by considering two auxiliary problems: The first problem deals with the axisymmetric indentation of a penny-shaped crack of radius b by a smooth rigid disc inclusion of radius a. Selvadurai and Singh (1984) presented an approximate solution to this problem, and the Mode I stress intensity factor at the boundary of the penny-shaped crack was evaluated as a series expansion in terms of the parameter $c(=a/b)$. The second auxiliary problem deals with the application of uniform internal pressure σ_0 to a penny-shaped crack of internal radius a and external radius b. Here again, the solution can be obtained in an approximate form as a series in terms of the parameter (a/b). This solution was developed by Selvadurai and Singh (1985) and a series expansion result can be obtained for the Mode I stress intensity factor at the external boundary of the annular crack. The radius of the zone of separation is obtained by the constraint that, at the boundary of separation, the combined stress intensity factors derived from the two auxiliary solutions should reduce to zero. This gives a characteristic equation in terms of c, which can be solved to determine the radius of the separation zone. The details of the analyses will be presented in a separate article (Selvadurai et al, 2018) and the method involves the estimation of the axial force $P_{\Delta v}$ induced on the circular patch due to the dilatant displacements Δv; the resulting expression takes the form

$$P_{\Delta v}=\frac{4aG\Delta v}{(1-\nu)}\left[\left(1+\frac{4c}{\pi}\right)+\frac{16c^2}{\pi^4}+c^3\left(\frac{64}{\pi^6}+\frac{16}{9\pi^4}-\frac{8}{9\pi^2}\right)+c^4\left(\frac{256}{\pi^8}+\frac{64}{9\pi^4}\right)+c^5\left(\frac{10240}{\pi^{10}}+\frac{9600}{225\pi^6}+\frac{92}{225\pi^2}\right)\right] \quad (1)$$

The shear stress required to attain failure of the interface experiencing Coulomb friction and dilatancy can be estimated using the failure concept proposed by Taylor (1948), which neglects any elastic energy of the interface and relates the external work of forces acting on the dilatant interfaces to the plastic energy dissipation. In Taylor's classic study, the dilatancy displacement Δv is related to the shear displacement Δu through a linear relationship that incorporates a constant dilatancy angle. In this research, the analysis is extended to include a non-linear relationship between Δv and Δu of the form

$$\Delta v=a\left(\frac{\Delta u}{a}\right)^2\left\{\exp\left(-\lambda\left|\frac{\Delta u}{a}\right|\right)\tan\alpha_0\right\} \quad (2)$$

where λ is a parameter that signifies degradation of the dilatancy due to processes such as asperity breakage and other micro-mechanical processes. The theoretical results enable the development of an expression for the amplification of the shear stress at the circular patch due to dilatancy effects. The "*Shear Stress Amplification Factor*" (*SSAF*) is expressed as

$$SSAF\quad\left(1+\frac{4G}{(1-\nu)\sigma_0\pi}\left(\frac{\Delta u}{a}\right)^2\exp\left(-\lambda\left|\frac{\Delta u}{a}\right|\right)\tan\alpha_0 P_N^{\Delta v}\right)\left(1+\frac{\Delta u}{a}\exp\left(-\lambda\left|\frac{\Delta u}{a}\right|\right)\frac{\tan\alpha_0}{\tan\varphi}\right) \quad (3)$$

The expression for *SSAF* takes into consideration the influence of the far-field normal stress σ_0 acting on the circular patch, the initial dilatancy angle α_0, the friction angle φ and the dilatancy degradation parameter λ. In the absence of dilatancy there is no amplification of

the rupture shear stress, i.e. $SSAF \to 1$. Figure 2 shows a typical result for the SSAF as a function of the normalized shear displacement $\Delta u / a$.

Concluding Remarks

The process of dilatancy can influence the attainment of the peak load capacity at a pre-compressed geological interface. The paper employs an elementary model for an interface where dilatancy is developed over a region with a circular planform. The elastic normal stiffness of the dilatant region is automatically accounted for in the mathematical developments. It is shown that the shear capacity of the dilatant circular region can be estimated using the procedure proposed by Taylor (1948). The enhancement of the shear capacity with dilatancy can be presented in the form of a non-dimensional relationship in which the case of Coulomb friction at the dilatant interface is the limiting case.

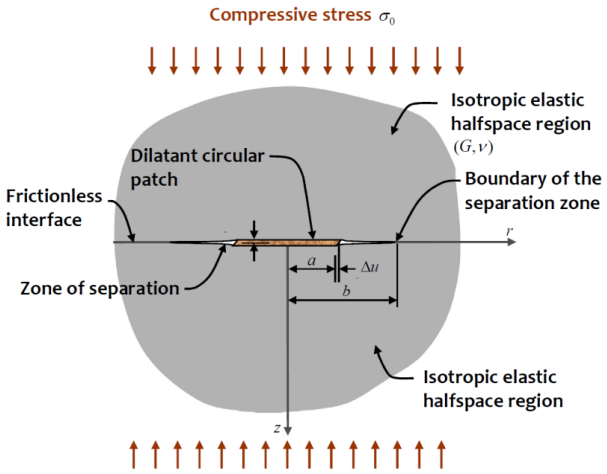

Figure 1. Indentation of halfspace regions due to dilatant processes over a circular patch.

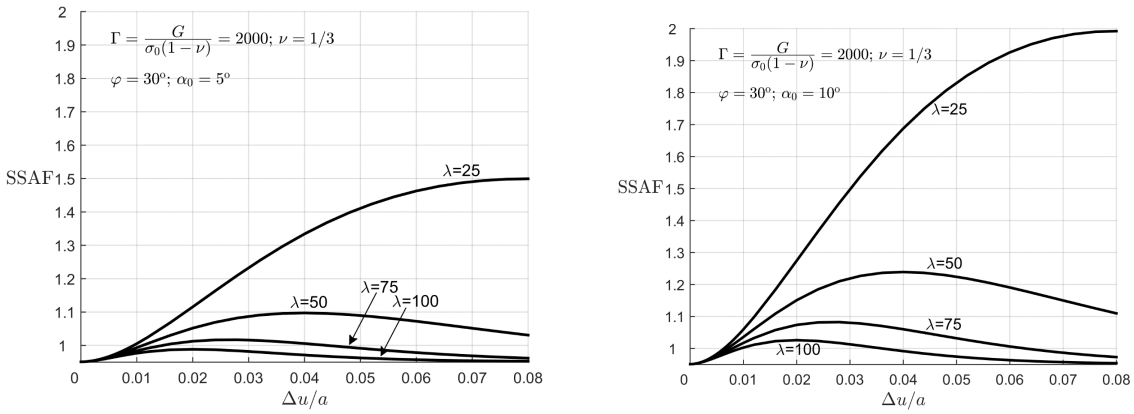

Figure 2. Dilatancy-induced shear stress amplification at a circular patch.

Acknowledgements

The work was supported by an *NSERC Discovery Grant* and the *James McGill Research Chairs Program*.

References

Desai CS, Christian JT (Eds.) 1977. *Numerical Methods in Geotechnical Engineering*, McGraw-Hill, New York.

Nguyen TS, Selvadurai APS1998. A model for coupled mechanical and hydraulic behavior of a rock joint. *International Journal for Numerical and Analytical Methods in Geomechanics,* **22**, 29–48.

Selvadurai APS Boulon MJ (Eds.) 1995. *Mechanics of Geomaterial Interfaces, Studies in Applied Mechanics* **42**, Elsevier, Amsterdam.

Selvadurai APS, Yu Q 2005. Mechanics of a discontinuity in a geomaterial. *Computers and Geotechnics* **32**, 92–106.

Selvadurai APS, Singh BM 1984. On the expansion of a penny-shaped crack by a rigid disc inclusion. *International Journal of Fracture*, **25**, 69–77.

Selvadurai APS, Singh BM 1985. The annular crack problem for an isotropic elastic solid. *Quarterly Journal of Mechanics and Applied Mathematics*, **38**, 233–243.

Selvadurai APS, Selvadurai PA, Suvorov, AP 2018. Shear of a dilatant patch at a compressed geological interface (*In preparation*)

Taylor DW (1948) *Fundamentals of Soil Mechanics*, John Wiley, New York.

Second-grade elasticity revisited: orthofibre theory

F. Froiio* & A. Zervos**

**Univ Lyon, École Centrale de Lyon, LTDS, F-69134, Ecully, France*
*** School of Engineering, University of Southampton, Highfield, Southampton SO17 1BJ, United Kingdom*
francesco.froiio@ec-lyon.fr

Dedicated to the memory of Ioannis Vardoulakis, Professor of Mechanics at NTU Athens, Greece, who initiated this research and contributed significantly to it till his untimely death.

The presentation targets two issues of relevance for the development of elastic theories in which the stored energy is assumed to depend on the first two gradients of the displacement (second-grade elastic materials). Our standpoint is expressed herein in the framework of linear elasticity. Nonetheless, the same results and concepts can be generalised to a large deformation analysis as well as to other constitutive frameworks.

A first, a long-standing issue concerns the additional boundary conditions arising for second-grade materials, namely as to their mechanical interpretation, the lack of which has caused second-grade theories to be viewed, hitherto, mostly as 'perturbations' of constitutive laws for simple (particularly 'first-grade') materials. The proposed developments are based on the concept of 'orthofibre' (Froiio et al., 2010, 2018), i.e. an infinitesimal material fibre approaching the boundary along the direction of the unit normal vector n_i. The relevant deformation measures, illustrated in Figure 1, are the orthofibre stretch and rotation fields:

$$\varsigma = n_i \, u_{(i,j)} \, n_j \qquad , \qquad \omega_{ij} = n_j \, u_{i,k} \, n_k - n_i \, u_{j,k} \, n_k \tag{1}$$

respectively. In particular, the axis of the infinitesimal rotation ω_{ij} lies orthogonal to n_i. On the basis of these definitions, the classical procedure of integration by parts (Mindlin, 1965) leads to the identification of the natural boundary conditions for second-grade elastic materials in the form of surface traction, 'ortho-fibre tension' and 'orthofibre couples' at regular points of the boundary as well as a line-traction at its edges. Orthofibre tension (i.e. force doublets normal to the boundary; see Bluestein, 1967) and couples are energy-conjugate to orthofibre stretch and rotations, respectively. The corresponding balance laws, which we identify by requiring objectivity of the relevant potential energies, are consistent with those exhibited by Fried & Gurtin (2006).

A second, strictly related issue pertains to the form of stress fields in the sense of Cauchy for second grade materials. After extending the definitions (1) to internal material surfaces, we propose an original derivation based on the classical 'cut argument': we define and calculate the relevant internal actions as reactive force-like fields in association with the 'constraint of continuity' of the displacement field and its first derivative across internal material surfaces. A first stress vector field is identified that has the same physical meaning as Cauchy's, but is dependent on the principal normal curvatures and on the relevant curvature directions of the internal surface; the same stress field degenerates on edges in the form of line-traction. Reactive orthofibre tension and couple fields are also identified along internal material surfaces, with a 'cubic' dependence on the unit normal 'n_i'. Therefore, a corresponding stress tensor in the classical sense can neither be postulated nor deduced for any of the above-mentioned stress fields (cf. Mindlin & Eshel, 1968). A number of common points, yet not a complete agreement, can be identified through the deductive procedure and the results of dell'Isola et al. (1995, 1997, 2012a, 2012b).

The interested reader may refer to Froiio & Zervos (2018) for a complete presentation of the above derivations, as well as for additional results concerning (i) an original representation of the linear isotropic elastic law for second-grade materials, (ii) three example boundary value problems, and (iii) the main lines of the finite element implementation of the theory.

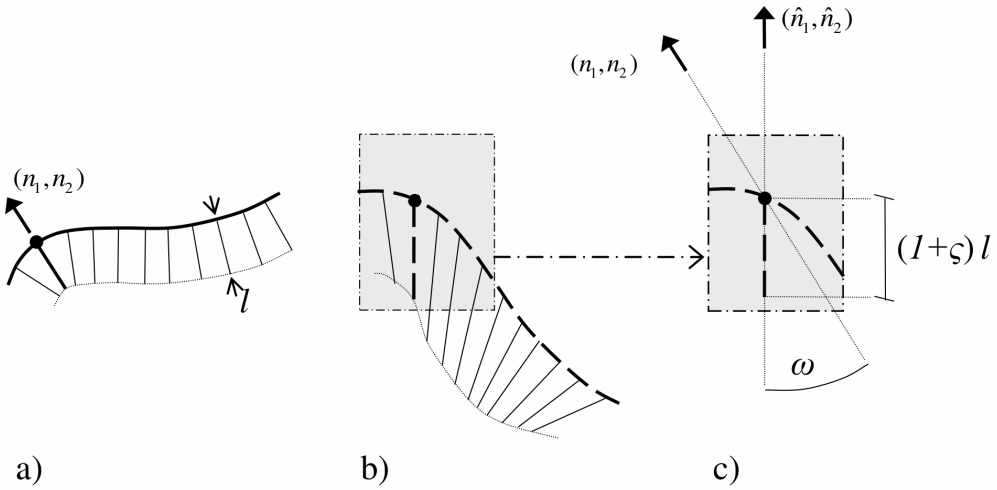

Figure 1. Orthofibres along an internal/boundary surface, 2-D representation: (a) reference configuration; (b) deformed configuration; (c) orthofibre stretch and -rotation

References

Bluestein, J. L., 1967. A note on boundary conditions of Toupin's second gradient theory. *International Journal of Solids and Structures*, 3, pp. 1053–1057.

dell'Isola, F. and Seppecher, P., 1995. The relationship between edge contact forces, double forces and insterstitial working allowed by the principle of virtual power. *Comptes rendus de l'Académie des Sciences – Series II b*, 321, pp. 303–308.

dell'Isola, F. and Seppecher, P. 1997. Edge contact forces and quasi-balanced power. *Meccanica*, 32, pp. 33–52.

dell'Isola, F., Madeo, A. and Placidi, L., 2012a. Linear plane wave propagation and normal transmission and reflection at discontinuity surfaces in second gradient 3D continua. *Zeitschrift für angewandte Mathematik und Mechanik*, 92, pp. 52-71.

dell'Isola, F., Seppecher, P. and Madeo, A., 2012b. How contact interactions may depend on the shape of Cauchy cuts in N-th gradient continua: approach "à la D'Alembert". *Zeitschrift für angewandte Mathematik und Physik*, 63, pp. 1119-1141.

Froiio, F., Zervos, A. and Vardoulakis, I., 2010. On natural boundary conditions in linear 2nd-grade elasticity. In: Maugin, G.A. and Metrikine, A.V. (eds.), *Mechanics of Generalized Continua – One hundred years after the Cosserats*, Springer, New York.

Froiio, F. and Zervos, A., 2018. Second-grade elasticity revisited. *Mathematics and mechanics of solids*, DOI: 10.1177/1081286518754616 (30 pages)

Fried, E. and Gurtin, M., 2006. Traction, balances and boundary conditions for nonsimple materials with applications to liquid flow at small-length scales. *Archive for Rational Mechanics and Analysis,* 182, pp.513–554.

Mindlin, R. D., 1965. Second gradient of strain and surface tension in linear elasticity. *International Journal of Solids and Structures*, 1, pp. 417–438.Mindlin, R. D. and Eshel, N. N., 1968. On first strain-gradient theory in linear elasticity. *Int. J. Solids Struct.*, 4, pp. 109–124.

Modelling the evolution of fabric anisotropy in granular materials

Chao-Fa Zhao[*,‡], Niels P. Kruyt[*]

[*] *Department of Mechanical Engineering, University of Twente, P.O. Box 217, 7500 AE Enschede, The Netherlands*

[‡] *LaSIE-UMR CNRS 7356, Université de La Rochelle, 23 Avenue Albert Einstein, 17000 La Rochelle, France*

E-mail: chaofa.zhao@gmail.com; n.p.kruyt@utwente.nl

Granular materials consist of a large number of grains and voids. The arrangement of particles, termed as internal structure influences significantly the behaviour of granular materials (Yoshimine *et al*., 1998; Kruyt, 2012; Kruyt & Rothenburg, 2016). For instance, packing A and packing B (shown in Fig. 1) consist of the same amount of particles even though they have different arrangements; their internal structures are therefore different. The internal structure of granular material is mostly characterized by fabric tensors (Oda, 1982; Li, 2016). Fabric tensors are statistical quantifications of microscale variables, such as contact normals, branch vectors or void vectors. Generally, the fabric tensor can be expressed as a second-order tensor $\mathbf{G}$:

$$\mathbf{G} = \frac{1}{2N}\sum_{k=1}^{2N} w(\mathbf{u}^k)\mathbf{u}^k \otimes \mathbf{u}^k \tag{1}$$

where $\mathbf{u}$ is an entity at microscale; $w(\mathbf{u})$ is a weight factor; $2N$ is the number of the entities to be quantified. Accordingly, the (evolution of) fabric anisotropy is described by the (evolution of) the deviatoric part of the second-order fabric tensor **G**.

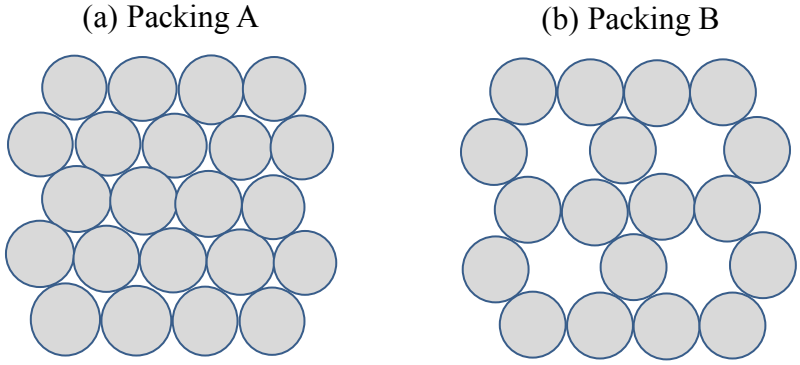

Figure 1. Different arrangements of the same amount of spherical particles.

The evolution of the fabric anisotropy in granular materials has been investigated by experimental tests (Yoshimine *et al*., 1998; Yang *et al*., 2008) as well as by Discrete Element Method (DEM) simulations (Kruyt, 2012; Kruyt & Rothenburg, 2014; Li, 2016; Yang & Wu, 2016). The results of the DEM simulations have clearly shown that the fabric anisotropy approaches asymptotic states under various loading conditions (Kruyt, 2012; Kruyt & Rothenburg, 2014). These observations are explicitly considered by the anisotropic critical state theory (Li & Dafalias, 2012) through the introduction into the classical critical state theory of a term that accounts for the fabric anisotropy. Recent DEM simulations (Kruyt, 2012; Zhao & Guo, 2013; Yang & Wu, 2016) have also shown that the initial void ratio, the inherent anisotropy and the Lode angle strongly affect the evolution of fabric anisotropy (Fig.2). However, the relations describing the evolution of fabric tensors in current constitutive models are heuristic, requiring the calibration of many model parameters.

Furthermore, current fabric evolution laws for granular materials are generally developed for continuum mechanical models (Gao & Zhao, 2017; Yang *et al*., 2018) by means of a loading index multiplier associated with the yield surface. These evolution laws cannot be employed in micromechanical models (Chang & Hicher, 2005; Hicher & Chang, 2006; Chang & Yin, 2009; Yin & Chang, 2009; Yin *et al*., 2010; Nicot & Darve, 2011; Misra & Singh, 2014; Zhao *et al*., 2018b) which do not have explicit macro-scale yield surfaces.

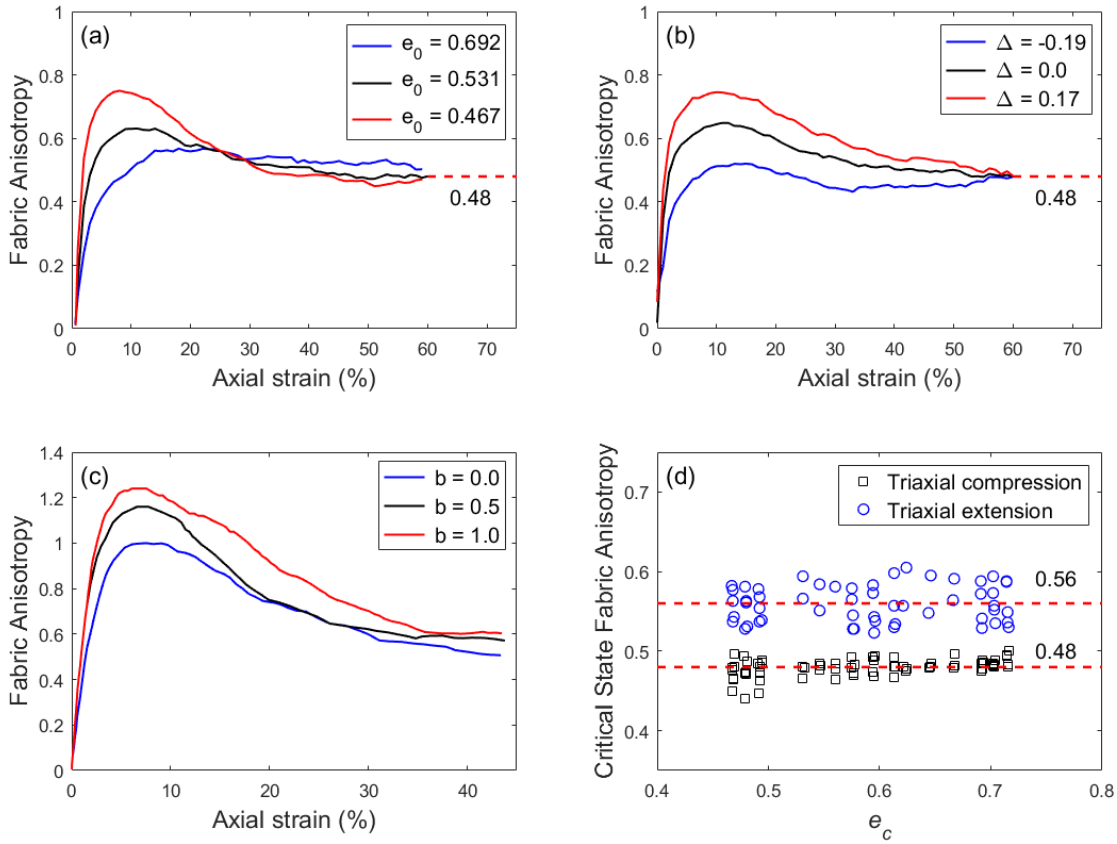

Figure 2. DEM simulations: (a) influence of initial void ratio e_0 on fabric evolution of an initially isotropic sample (data from Yang & Wu, 2016); (b) influence of inherent anisotropy Δ on fabric evolution of a dense-medium sample (e_0=0.531) under confining pressure of 500 kPa (data from Yang & Wu, 2016); (c) influence of intermediate principal stress ratio b-value on fabric evolution of an initially isotropic sample (data from Chantawarangul, 1993); (d) influence of loading direction on critical state fabric anisotropy of an initially isotropic sample (data from Yang & Wu, 2016).

Given these limitations and the fact that micromechanics-based constitutive relations have been successfully employed in solving engineering problems (Zhao *et al*., 2018a; 2018c), it is important to consider properly the evolution of the fabric tensor in both continuum and micromechanical modelling of granular materials. This study proposes an evolution law for fabric anisotropy based on observations from experiments and DEM simulations and suggests its effectiveness in micromechanical modelling of granular materials.

References

Chang, C. S. and Hicher, P. Y., 2005. An elasto-plastic model for granular materials with microstructural consideration. *International Journal of Solids and Structures*, 42(14), pp. 4258-4277.

Chang, C. S. and Yin, Z. Y., 2009. Micromechanical modeling for inherent anisotropy in granular materials. *Journal of Engineering Mechanics*, 136(7), pp. 830-839.

Chantawarangul, K., 1993. Numerical simulations of three-dimensional granular assemblies. Ph. D. Thesis, Department of Civil Engineering, University of Waterloo.

Gao, Z. and Zhao, J., 2017. A non-coaxial critical-state model for sand accounting for fabric anisotropy and fabric evolution. *International Journal of Solids and Structures*, 106, pp. 200-212.

Hicher, P. Y. and Chang, C. S., 2006. Anisotropic nonlinear elastic model for particulate materials. *Journal of Geotechnical and Geoenvironmental Engineering*, 132(8), pp. 1052-1061.

Kruyt, N. P., 2012. Micromechanical study of fabric evolution in quasi-static deformation of granular materials. *Mechanics of Materials*, 44, pp. 120-129.

Kruyt, N. P. and Rothenburg, L., 2014. On micromechanical characteristics of the critical state of two-dimensional granular materials. *Acta Mechanica*, 225(8), pp. 2301-2318.

Kruyt, N. P. and Rothenburg, L., 2016. A micromechanical study of dilatancy of granular materials. *Journal of the Mechanics and Physics of Solids*, 95, pp. 411-427.

Li, X., 2016. Internal structure quantification for granular constitutive modeling. *Journal of Engineering Mechanics*, 143(4), pp. C4016001.

Li, X. S. and Dafalias, Y. F., 2011. Anisotropic critical state theory: role of fabric. *Journal of Engineering Mechanics*, 138(3), pp. 263-275.

Misra, A. and Singh, V., 2014. Nonlinear granular micromechanics model for multi-axial rate-dependent behavior. *International Journal of Solids and Structures*, 51(13), pp. 2272-2282.

Nicot, F. and Darve, F., 2011. The H-microdirectional model: accounting for a mesoscopic scale. *Mechanics of Materials*, 43(12), pp. 918-929.

Oda, M., 1982. Fabric tensor for discontinuous geological materials. *Soils and Foundations*, *22*(4), pp.96-108.

Yang, Z. X., Li, X. S. and Yang, J., 2008. Quantifying and modelling fabric anisotropy of granular soils. *Géotechnique*, 58(4), pp. 237-248.

Yang, Z. X. and Wu, Y., 2016. Critical state for anisotropic granular materials: a discrete element perspective. *International Journal of Geomechanics*, 17(2), pp. 04016054.

Yang, Z. X., Xu, T. T. and Chen, Y. N., 2018. Unified modeling of the influence of consolidation conditions on monotonic soil response considering fabric evolution. *Journal of Engineering Mechanics*, 144(8), p.04018073.

Yin, Z. Y. and Chang, C. S., 2009. Microstructural modelling of stress-dependent behavior of clay. *International Journal of Solids and Structures*, 46(6), pp.1373-1388.

Yin, Z. Y., Chang, C. S. and Hicher, P. Y., 2010. Micromechanical modelling for effect of inherent anisotropy on cyclic behaviour of sand. *International Journal of Solids and Structures*, 47(14-15), pp. 1933-1951.

Yoshimine, M., Ishihara, K. and Vargas, W., 1998. Effects of principal stress direction and intermediate principal stress on undrained shear behavior of sand. *Soils and Foundations*, 38(3), pp. 179-188.

Zhao, C. F., Yin, Z. Y. and Hicher, P. Y., 2018a. Integrating a micromechanical model for multiscale analyses. *International Journal for Numerical Methods in Engineering*, 114(2), pp. 105-127.

Zhao, C. F., Yin, Z. Y., Misra, A. and Hicher, P. Y., 2018b. Thermomechanical formulation for micromechanical elasto-plasticity in granular materials. *International Journal of Solids and Structures*, 138(5), pp. 64-75.

Zhao, C. F., Yin, Z. Y. and Hicher, P. Y., 2018c. A multiscale approach for investigating the effect of microstructural instability on global failure in granular materials. *International Journal for Numerical and Analytical Methods in Geomechanics*.

Zhao, J. and Guo, N., 2013. Unique critical state characteristics in granular media considering fabric anisotropy. *Géotechnique*, 63(8), pp. 695-704.

DEM-FEM coupling method to simulate thermally induced stresses and local damage in composite materials

W. Leclerc*, H. Haddad & M. Guessasma***

** Laboratoire des Technologies Innovantes, EA 3899, F-02100, Saint-Quentin, France.*
*** "Institute of Research for Ceramics, UMR 7315, F-87068, Limoges, France.*
willy.leclerc@u-picardie.fr

The present work proposes a coupling method combining finite and discrete elements to simulate thermally induced stresses and local damage in composite materials. Ceramic-metal materials characterized by a strong difference of properties and a Coefficient of Thermal Expansion (CTE) mismatch have been investigated. Typically, thermal residual stresses are induced at the interface during a cooling process which can lead to catastrophic effects on the local integrity of the joint. Recently, a Discrete Element Method (DEM) based on a hybrid particulate-lattice description was successfully introduced to simulate these effects. Such an approach profits from a cohesive beam element to model effective continuous media (Fig. 1) with monitored microscopic parameters in which complex damage effects can be introduced (Haddad & Leclerc 2015, Leclerc & Haddad 2017).

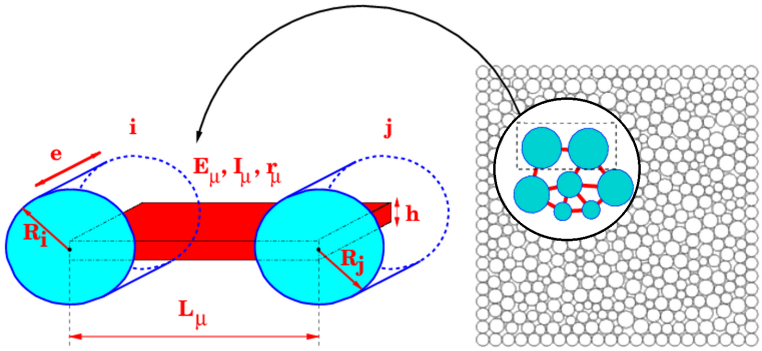

Figure 1. Cohesive model based on Euler-Bernoulli beam element

However, full discrete simulations which require massive calculations and prohibitive calculation costs renders this method unlikely to be commonly used. As a result, a coupling method successively combining both the continuous and discrete approaches has the advantage of being less expensive. In this work, we have investigated the DEM-FEM coupling approach based on a domain decomposition with an overlapping area (Haddad & Guessasma 2014) which has already proved to be flexible and reliable in a large context. Preliminary studies were first carried out to verify the accuracy of our implementation in our MULTICOR++ code through classical tensile tests (Fig 2).

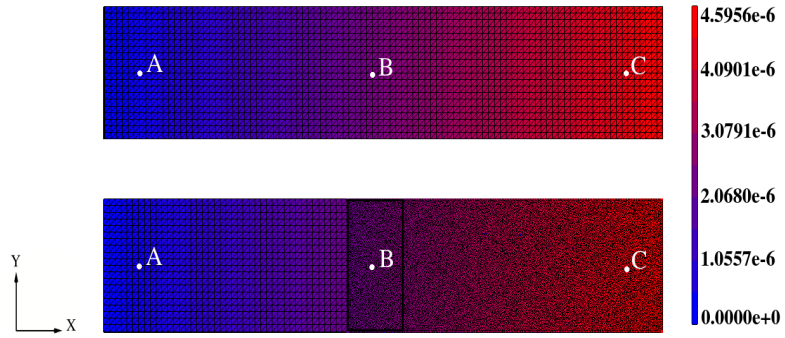

Figure 2. Comparison of the displacement field between FEM and DEM-FEM simulations.

In a second step, a model of thermal expansion based on the natural dilatation of each beam element (André 2017) was introduced into the discrete model. Tests were performed in the framework of ceramic-metal fiber composites using a 2D representative pattern composed of 15 dilute inclusions. In the coupling method, the matrix was globally discretized by a finite element mesh while a circular discrete area was placed around each heterogeneity where local stress peaks and damage could occur. Comparisons in terms of stress and strain fields exhibited the efficiency of the coupling method to take into account such thermal effects with a suitable accuracy (Fig. 3). Moreover, in comparison to FEM and DEM, they also showed a significant decrease in computation time.

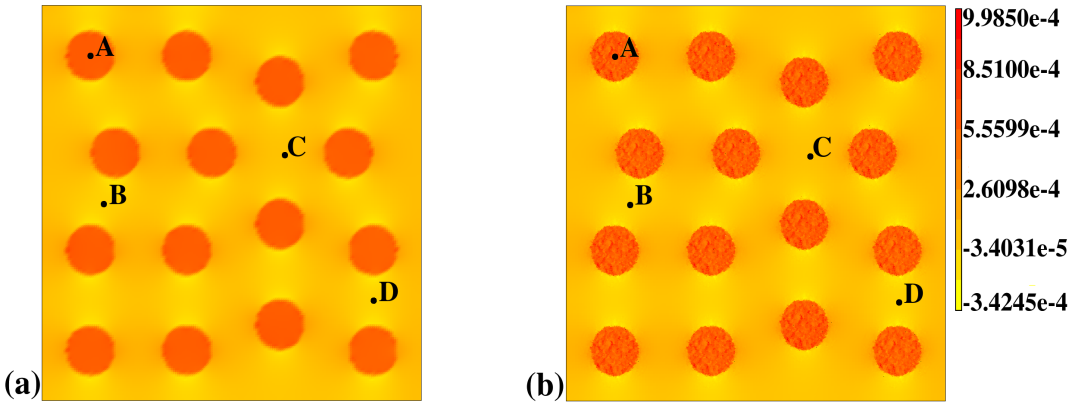

Figure 3. Elastic strain field obtained by (a) FEM and (b) DEM-FEM method

Based on these encouraging results, interfacial effects were also introduced using the Discrete Damage Zone Model (Liu, 2012) to exhibit the local damage related to the CTE mismatch during a cooling process. The flexibility of such an approach was also evident in studies which considered problems such as the classical ceramic-metal joint issue. Therefore, in the future, we expect to extend this approach to multi-physical behaviours. More specifically, we aim to develop efficient numerical methods to consider thermo-elastic and thermo-electrical couplings in heterogeneous media.

References

Haddad, H., Leclerc, W. and Guessasma, M., 2015. Application of DEM to predict the elastic behavior of particulate composite materials. *Granular Matter*, 17, pp. 459-473.

Leclerc, W., Haddad, H. and Guessasma, M., 2017. On the suitability of a Discrete Element Method to simulate cracks initiation and propagation in heterogeneous media. *International Journal of Solids and Structures*, 108, pp. 98-104.

Haddad, H., Guessasma, M. and Fortin, J., 2014. Heat transfer by conduction using DEM–FEM coupling method. *Computational Materials Science*, 81, pp. 339-347.

André, D., Levrault, B., Tessier-Doyen, N. and Huger M., 2017. A discrete element thermo-mechanical modelling of diffuse damage induced by thermal expansion mismatch of two-phase materials. *Computer Methods in Applied Mechanics and Engineering*, 318, pp. 898-916.

Liu, X., Duddu, R. and Waisman, H., 2012. Discrete damage zone model for fracture initiation and propagation. *Engineering Fracture in Mechanics*, 92, pp. 1-18.

Studying flow control with reduced order models

C. Allery & A. Tallet

LaSIE UMR CNRS 7356, Université de La Rochelle
Avenue Michel Crépeau, 17041 La Rochelle Cédex 01
callery@univ-lr.fr

Given its many industrial applications in aeronautics, aerodynamics, fluid mechanics, civil engineering, etc, the subject of flow control is highly important. However, for researchers the subject is also challenging because the use of iterative algorithms required in terms of CPU time and memory makes it extremely costly. In the order to decrease these costs, we have developed Reduced Order Models (ROM) which consist of putting most of the heavy calculations offline, while keeping only fast fluid flow evaluations online.
Here we focus on the control of indoor air quality: a temperature profile is kept in a room by the interaction of the intensity and temperature of the injected air. The aim is thus to minimize the difference between the target temperature $\hat{\theta}$ and the indoor temperature θ. This is achieved by minimizing the following cost functional:

$$\mathcal{J}(\theta,\alpha,\sigma) = \frac{1}{2}\int_{\Omega}\int_{0}^{T}(\theta(\mathbf{x},t)-\hat{\theta}(\mathbf{x},t))^2 d\mathbf{x}dt + \frac{\omega_1}{2}\alpha^2 + \frac{\omega_2}{2}\sigma^2 \quad (1)$$

under the constraints of Navier-Stokes equations and the convection-diffusion equation respectively noted N(u,θ,α,σ)=0 and M(u,θ,α,σ)=0. u corresponds to the velocity. The control parameters α and σ monitor, respectively, the values of the inlet velocity and of the wall temperature. ω_1 and ω_2 are penalty terms of the objective functional to regularize the optimization problem.
The model reduction technique consists of searching a reduced spatial basis Φ(x) such as the solution h(x, t) (h denotes the velocity or temperature) of the problem can be approximated by $h(x,t)\approx\sum_{i=1}^{N} c_i(t)\Phi_i(x)$, where N is considerably smaller than the number of degrees of freedom arising from classical methods such as the Finite Element method or the Finite Volume method. The POD (Proper Orthogonal Decomposition) is the most commonly used technique to construct the spatial basis Φ(x). Here each quantity (velocity and temperature field) is decomposed into a mean part and a fluctuating part upon which the POD has been applied:

$$u(x,t,\alpha,\sigma)=u(x,\alpha,\sigma)+u'(x,t,\alpha,\sigma) \quad \text{and} \quad \theta(x,t,\alpha,\sigma)=\theta(x,\alpha,\sigma)+\theta'(x,t,\alpha,\sigma) \quad (2)$$

with $u'(x,t,\alpha,\sigma)\approx\sum_{i=1}^{Nu} a_i(t,\alpha,\sigma)\,\Phi^u_i(x)$ and $\theta'(x,t,\alpha,\sigma)\approx\sum_{i=1}^{Nt} b_i(t,\alpha,\sigma)\,\Phi^t_i(x)$ (3)

Theses POD bases are constructed from numerical simulations for several values of the inlet fluid velocity and wall temperature i.e. for various parameters α_i and σ_i,
Once the spatial POD bases have been computed, the dynamical of the velocity and the temperature can be obtained by solving a Reduced Order Model (ROM) constituted of a set of differential equations in a_i and b_i, of small size N_u+N_t. For this ROM to be developed, the expressions of the velocity and temperature fields (Equ. 2 and 3) are first introduced into the Navier-Stokes and the convection-diffusion equations. The reduced model is then obtained by

Galerkin projection of the resulting equations onto the POD modes. To increase the robustness of the POD-ROM, it is necessary to adapt the mean fields which appear in the ROM by using a Lagrange interpolation on the parameters α and σ. For more details see (Tallet et al, 2016).

The ROM is now embedded in a control loop. For this to be realized, the full optimization problem, described in the beginning of the summary, has been turned into a reduced optimization problem which consists of seeking the control parameters α and σ which minimizes the difference between the target temporal coefficient $\hat{\mathbf{b}}(t,\alpha,\sigma)$ and the temporal coefficient b(t,α,σ) associated to the temperature field. In this case, the state variables correspond to the time-dependent coefficients a(t,α,σ) and b(t, α,σ). The reduced objective functional $J_r(b,\alpha,\sigma)$, is expressed in terms of the reduced variable b(t,α) and the control parameters α and σ by introducing the decomposition (Eq. 2 and 3) into the functional J(θ,α,σ), (Eq. 1) and using the orthonormality property of the POD-basis functions

$$\mathcal{J}_r(\mathbf{b},\alpha) = \frac{1}{2}\sum_{i=1}^{N^\theta}\int_0^T (b_i - \hat{b}_i)^2\,\mathrm{d}t + \frac{1}{2}\sum_{i=1}^{N^\theta}(b_i|_T - \hat{b}_i|_T)^2 \cdot \tag{4}$$

This functional must now be minimized under the reduced constraint equations, i.e. the ROM. This constrained optimization problem is converted into an unconstrained optimization problem by the use of the Lagrange multipliers method and is solved by an iterative descent method (Bergman & Cordier, 2008) (Oulghelou & Allery, 2018),

This approach was applied to control the temperature in a lid-driven square cavity heated from the left side. The fluid flow is incompressible in the volume Ω of length L (Figure 1). The cavity is driven by the top with intensity U_0. Hot and cold temperatures (respectively, θ_h and θ_c) are, respectively, imposed on the left and right walls and the other walls are considered as adiabatic. The optimal flow control is realized on the boundaries; i.e., the lid velocity and the hot temperature imposed on the left wall, such as: $u_{top}=\alpha U_0$ and $\theta_{left}=\sigma\,\theta_h$. α and σ are the control parameters.

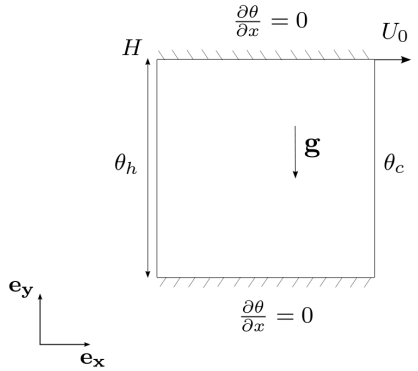

Figure 1. Boundary conditions of the lid-driven cavity heated on the left.

In the following, the Reynolds number is defined as $Re=\alpha U_0/\nu$ and the Grashof number as $Gr = g\beta L^3(\sigma\theta_h-\theta_c)/\nu^2$. ρ is the density, ν the kinematic viscosity, g the gravitational acceleration and β the volumetric thermal expansion coefficient. The streamlines and isovalues of temperature, at a given time, are drawn in figure 2.

The POD bases (of velocity and temperature) are constructed with snapshots from 6 simulations for six couples of (Re,Gr) such as Re=158; 316; 474 and $Gr=10^6$; $5x10^6$. For each couple (Re,Gr), 150 snapshots evenly distributed on the transient regime are considered. These bases are used to construct the ROM required to solve rapidly the reduced control problem. The aim is thus to achieve a target temperature θ_{targ} corresponding to a couple

(Re_{targ},Gr_{targ}) by starting from an initial temperature θ_{init} corresponding to (Re_{init},Gr_{init}). Four target pairs of (Re,Gr) that do not belong to the sampling are considered : 1) Re = 221 - Gr = $2x10^6$; 2) Re = 221 ; Gr = $4x10^6$; 3) Re = 379 ; Gr = $2x10^6$ 4) Re = 379 ; Gr = $4x10^6$.

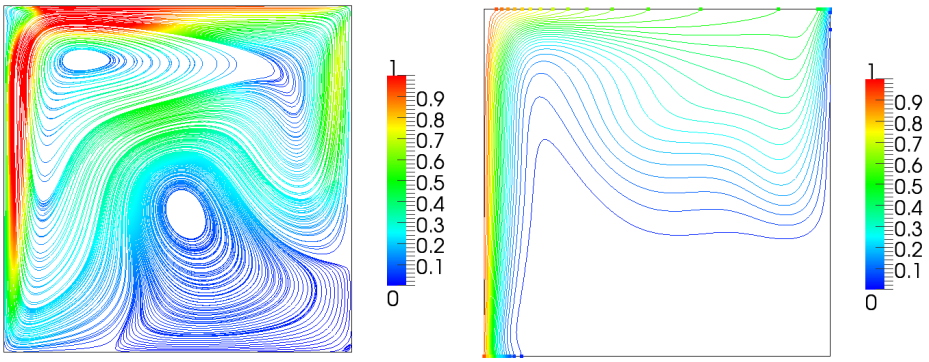

Figure 2. Streamlines and isocontours of temperature at t=3s for Re=316 and Gr=$1x10^6$

The control algorithm converges quickly (around a few minutes on a cluster) towards the target control parameters (Reynolds and Grashof numbers) in twenty iterations maximum (see Figure 3). The time-average relative error, between the fields issued from the full model and those obtained at the end of the algorithm control is about 13% for the velocity and 5% for the temperature. The reduced control algorithm can then be considered as fast and accurate.

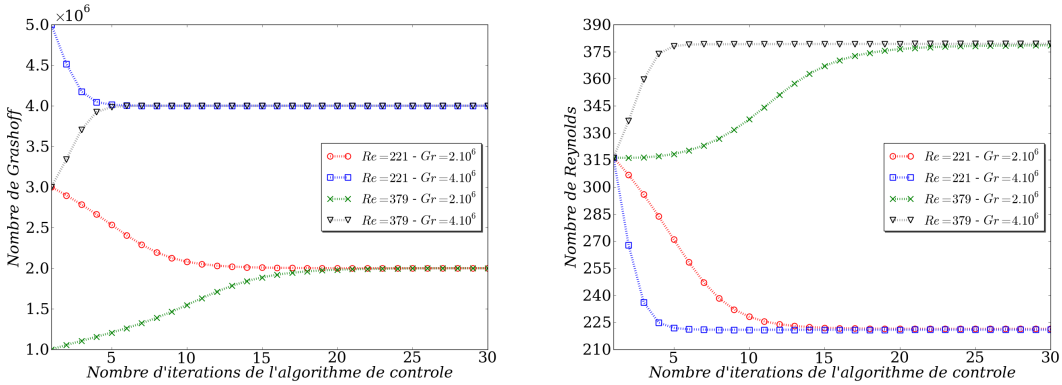

Figure 3. Grashof number Gr and Reynolds number Re as a function of the iterations number of the control algorithm for each target.

References

Bergmann M. and Cordier L., 2008. Optimal control of the cylinder wake in the laminar regime by trust-region methods and POD reduced-order models. *Journal of Computational Physics*, 227(16), pp 7813–7840.

Tallet A., Allery C., and Leblond C., 2016. Optimal flow control using a pod-based reduced-order model, *Numerical Heat Transfer Part B Fundamentals*, 6, pp.1–24.

Oulghelou M. and Allery C., 2018. A fast and robust sub-optimal control approach using reduced order model adaptation techniques, *Applied Mathematics and Computation*, 333, pp. 416 – 434.

Gradient corrected SPH applied to coupled systems

Johannes Joubert, Nico Wilke, Patrick Pizette, Nicolin Govender, Nor-Edine Abriak

**IMT Lille Douai, Univ. Lille, EA 4515 - LGCgE - Laboratoire de Génie Civil et géoEnvironnement, département Génie Civil & Environnemental, F-59000 Lille, France*
*** Department of Chemical Engineering, University of Surrey, United Kingdom*
****Centre of Asset and Integrity Management, University of Pretoria, South Africa*
Email "Johannes Joubert" u10688944@tuks.co.za and johannes.joubert@imt-lille-douai.fr

In recent years, the rapid development of general purpose GPU (GP-GPU) has allowed the huge computational resources available on GPUs to be exploited for parallelizable tasks. Due to the architecture of GPUs focusing heavily on computation power in the form of computational cores at the cost of a more generalized control circuit, parallelizable tasks are those which require many independent operations but with the same logical structure. When considering the binary short-ranged particle interactions typically found in the discrete element method (DEM), clearly DEM particle contact, forcing calculation, and integration are all examples of massively parallelizable tasks. In fact, it has been shown that for industrial scale problems with particle numbers in the several millions, huge performance benefits can be seen by exploiting the vast computational resources available from GP-GPUs [1].
With this in mind, the Blaze-DEM framework is an implementation of a DEM solver developed using the NVIDIA CUDA C/C++ toolkit [1, 2]. While DEM excels at modelling particulate systems, many of these systems cannot be explicitly modelled in isolation. Many granular applications make use of wetted particles, whereby the systems behaviour is strongly influenced by a fluid interacting with the system. Several examples of such systems can be found in industry such as concrete mixing, sediment management, or soil erosion. Usually for low concentrations of fluid, this can be accounted for with cohesion models; however, this strategy cannot be used for fluid dominated flows. Furthermore, fluid interaction is not the only continuum interaction that plays crucial roles in several particulate system interactions with kiln drying and blast furnaces both serving as an example of particle-fluid-heat interactions. Finally, when considering the resolution of particle contact using some form of particle penetration, if we want to know the detail stress fields inside DEM particle or at boundaries, a further elastic continuum field needs to be resolved. Using the Blaze-DEM framework as a foundation, the goal of this study is to extend its capabilities by implementing a partial differential equation (PDE) solver that interacts in a monolithic fashion with Blaze-DEM.
In order to operate on the same scale as the DEM solver, this PDE solver will also need to be parallelizable. As such, the chosen solution strategy is a modification of the smoothed particle hydrodynamics (SPH) method first proposed in 1977 by Gingold and Monagham [3]. SPH is a solution strategy that makes use of continuum ”particles” that are free to move while carrying local information with them. In order to propagate the particles point-wise information into the system, SPH relies on the following identity:

$$f(\boldsymbol{x}) = \int_{\mathbb{R}} f(\boldsymbol{x})\delta(\boldsymbol{x} - \boldsymbol{x})dV = \int_{\mathbb{R}} f(\tilde{\boldsymbol{x}})W(\boldsymbol{x} - \tilde{\boldsymbol{x}}, h)dV$$

where W(x, h) is some approximation that tends to δ(x) in the limit as h → 0. Discretizing the integral leads to the actual function approximation of SPH. With this formulation in mind, it becomes clear that SPH uses a Lagrangian frame to track the continuum, as opposed to the

more common Eulerian frame commonly employed in other solution strategies such as the finite volume of finite difference methods. Opposed to many other studies making use of ghost particles [4] or variations of it such as making use of extrapolated fixed point values [5, 6, 7, 8], this solver makes use of a boundary implementation as proposed by Hashimi et al [9]. This method makes use of truncation, whereby the SPH differential approximations are expanded under a Taylor series expansion and permit the leading error terms to be truncated by means of a linear operator. This operation, while reducing the error in spatial discretization, also alleviates the problems associated with having a reduced number of particles at the boundary and improves gradient approximations at the DEM particle surfaces. Using this information, the SPH equations of motion are inverted allowing for the recovery of surface pressures consistent with the DEM particles acceleration. Furthermore, while not directly evident, this is only a specific case of a generalized mixed boundary condition and, as such, this method can be used to implement Neumann boundary conditions such as fixed heat flux or symmetry boundary conditions or even other generalized boundary conditions such as convection boundaries.

This approach has been applied to various 2D and 3D problems such as flow over a cylinder, heated porous cavity, Rayleigh-Taylor instability, dam break with obstacles and accelerating particles in a bath. Presented below in Figure 1 is an example showcasing the type of results obtained with the proposed methodology applied specifically to buoyancy driven flow in a porous media. All boundaries of the surrounding box are set to enforce adiabatic conditions while the boundaries of the spheres are kept at a fixed temperature. All solid interfaces have no-slip boundary conditions. Complex flow behaviour is observed with clear reflow zones occurring in several locations due to large velocity gradients trapping the fluid locally and exchanging heat between the high velocity fluid and the solids, generating vortices at the near the porous boundary interfaces. This illustrates the force of this solution strategy showing the capability of this method to handle complex geometries with two-way multiphysics coupling.

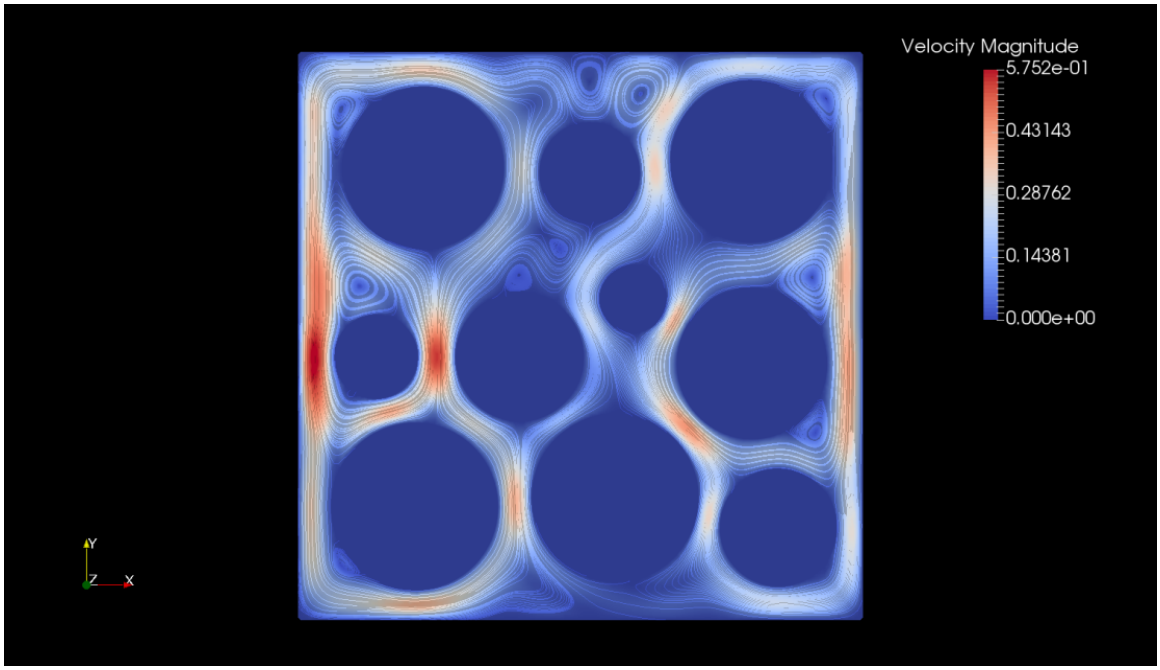

Figure 1: Velocity streamlines of buoyancy driven cavity

References

[1] Nicolin Govender, Daniel N. Wilke, and Schalk Kok. “Collision detection of convex polyhedra on the NVIDIA GPU architecture for the discrete element method”. In: Applied Mathematics and Computation 267 (2015). The Fourth European Seminar on Computing (ESCO 2014), pp. 810–829.

[2] Nicolin Govender, Daniel N. Wilke, and Schalk Kok. “Blaze-DEMGPU: Modular high performance DEM framework for the GPU architecture”. In: SoftwareX 5 (2016), pp. 62–66.

[3] R. A. Gingold and J.J. Monaghan. “Smoothed particle hydrodynamics: theory and application to non-spherical stars”. In: Monthly Notices of the Royal Astronomical Society 181.3 (1977), pp. 375–389.

[4] L.D. Libersky and A.G. Petschek. “Smooth particle hydrodynamics with strength of materials”. In: Advances in the Free-Lagrange Method Including Contributions on Adaptive Gridding and the Smooth Particle Hydrodynamics Method. Berlin, Heidelberg: Springer, 1991, pp. 248–257.

[5] S. Marrone, M. Antuono, A. Colagrossi, G. Colicchio, D. Le Touzfffdfffd, and G. Graziani. “δ-SPH model for simulating violent impact flows”. In: Computer Methods in Applied Mechanics and Engineering 200.13-16 (2011), pp. 1526–1542.

[6] B. Bouscasse, A. Colagrossi, S. Marrone, and M. Antuono. “Nonlinear water wave interaction with floating bodies in SPH”. In: Journal of Fluids and Structures 42 (2013), pp. 112–129.

[7] Y. Chen, X. Zheng, S. Jin, and W. Duan. “A corrected solid boundary treatment method for Smoothed Particle Hydrodynamics”. In: China Ocean Engineering 31.2 (2017), pp. 238–247.

[8] A.D. Chow, B.D. Rogers, S.J. Lind, and P.K Stansby. “Incompressible SPH (ISPH) with fast Poisson solver on a GPU”. In: Computer Physics Communications 226 (2018), pp. 81–103.

[9] M. R. Hashemi, R. Fatehi, and M. T. Manzari. “A modified SPH method for simulating motion of rigid bodies in Newtonian fluid flows”. In: International Journal of Non-Linear Mechanics 47.6 (2012), pp. 626–638.

Multiscale modelling for long-Term creep of concrete considering the interfacial transition zone surrounding the aggregate

F. Grondin & M. Guo

Institut de Recherche en Génie Civil et Mécanique, GeM - UMR 6183, Centrale Nantes – Université de Nantes - CNRS, 1 rue de la Noë, F-44321 Nantes, France
E-mail: *frederic.grondin@ec-nantes.fr*, *menghuan.guo@ec-nantes.fr*
webpage: https://www.ec-nantes.fr

This work analyses the influence exerted by the weak area surrounding the aggregate in concrete, the Interfacial Transition Zone (ITZ), upon the long-term creep behaviour of concrete. To simulate the behaviour of concrete, many researchers have treated concrete as a two-phase material consisting of mortar matrix and aggregates. However, there is another phase known as ITZ which is considered to be the weakest zone in concrete and, therefore, responsible for its fragility. ITZ is formed during the mixing process of concrete: before adding water into the mixture, cement grains are in contact with aggregates and are maintained in contact for some of them after adding water and during the mixing. So, a small area around the aggregate is formed where the hydration of cement is not the same as the hydration at a certain distance from the aggregate. In most cases, this area shows lower mechanical properties due to higher porosities. Under loading, micro-cracks can appear more easily around the aggregates in concrete. Also, since concrete is a viscoelastic material, it will show delayed deformations under a constant load which can lead to cracking. The micro-cracks caused by creep can be detrimental to the efficiency of concrete. In civil engineering, it is of great interest to understand the creep behaviour of concrete. For a long period (up to several dozen years), it was not possible to perform experimental creep tests and numerical models, therefore, provided the only viable method. The main theory of creep of concrete considered that the main hydrate of the cement paste, Calcium Silicate Hydrate (C-S-H), is strongly linked to the viscoelastic behaviour (Bažant and Prasannan, 1988a). The experimental tests showed that it deforms under a constant load and these deformations are restrained by the presence of aggregates, which cause the creation of micro-cracks in the cement paste.

Many macroscopic models have been developed for long-term creep of concrete. But missing is a study of the influence of viscoelasticity of the ITZ on the creep of concrete. The only way to add it into a model is to consider it explicitly in a volume. Hence, macroscopic models cannot be used. Indeed, the ITZ thickness (20 to 50 μm) is very small and can be distinguished by many layers with different characteristics. Given the limits of the calculation ability of the computer, it was suggested by Grondin and Matallah (2014) to calculate the properties of each layer by a hydration model (Grondin et al., 2010) and then to homogenize them. In a finite element code, the ITZ can be considered as a homogenous phase surrounding the aggregate. Also, according to the volume size of the concrete and the minimum size of the elements, a second homogenization could be performed by adding a part of the bulk cement paste or mortar to obtain an Effective Mixed Interphase (EMI) (Grondin and Matallah, 2014) with lower properties than the bulk mortar (Figure 1). This method allows the weakest area around the aggregate to be considered.

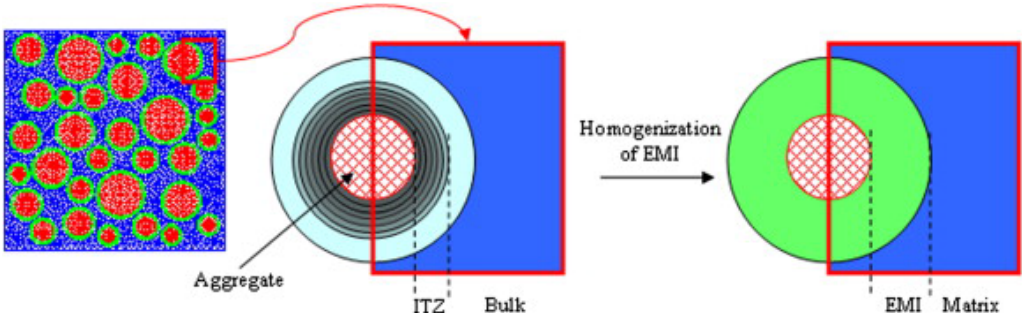

Figure 1. Definition of the Effective Mixed Interphase (Grondin and Matallah, 2014).

In this study, we propose a multi-scale model of concrete considering the ITZ in order to simulate the long-term creep behaviour of concrete. Four scales have been considered (Farah et al., 2017): 1) {C-S-H + pores}, 2) cement paste formed by {C-S-H + pores} and {other hydrates + residual clinkers}, 3) mortar formed by {cement paste} and {sand grains}, 4) concrete formed by {mortar} and {aggregates}. These scales have been chosen according to the representative elementary volume definition. At scales 1 and 2, the hydration model (Grondin et al., 2010) is used to calculate the volume fractions of the cement paste phases. At scale 1, the formula of Ricaud and Masson (2009) is applied to calculate the effective viscoelastic properties ($k_{\downarrow}\mathbf{1}^{\uparrow}i$) from that of C-S-H ($k_{\downarrow}CSH^{\uparrow}i$) and the pores volume fraction ($f_{\downarrow}p$) :

$$k_{\mathbf{1}}^{i} = k_{CSH}^{i}\frac{4(1-f_p)}{3f_p}$$

At scales 2, 3 and 4, the inclusions are randomly distributed in the volume and a finite element code is used to calculate the effective creep compliance $J^{\mathbf{hom}(t)}$ (Tran et al., 2011) from the average strain $\langle\varepsilon(t,y)\rangle_V$ and the average stress $\langle\sigma(t,y)\rangle_V$ (Farah et al., 2017):

$$\langle\varepsilon(t,y)\rangle_V = J^{\mathbf{hom}(t)}:\langle\sigma(t,y)\rangle_V$$

At the concrete scale, ITZ is considered around the aggregate and a constant load is applied to the volume. We can simulate the compressive and tensile creep behaviour by coupling a damage model to follow the crack growth during the test. Simulations were performed for a creep loading of 100 years and results are presented in Figure 2 for the ITZ properties equal to 0.1 to 0.8 times the values of the bulk mortar. We have noticed that the presence of the ITZ influences the creep displacements and the lower its properties, the higher the displacements will be with risk of cracking.

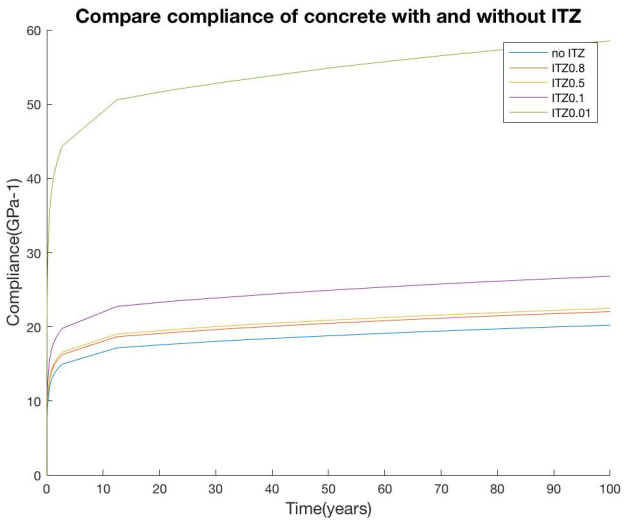

Figure 2. Calculation of the tensile creep compliances of concrete for different ITZ properties.

References

[1] Z.P. Bažant and S. Prasannan, Solidification theory for aging creep, *Cem. Concr. Res*., **18**, 923-932, (1988).

[2] F. Grondin and M. Matallah, How to consider the Interfacial Transition Zones in the finite element modelling of concrete?, *Cem. Concr. Res*., **58**, 67–75, (2014).

[3] F. Grondin, M. Bouasker, P. Mounanga, A. Khelidj and A. Perronnet, Physico-chemical deformations of solidifying cementitious systems: multiscale modelling, *Mater. Struct*., **43** (1), 151–165, (2010).

[4] M. Farah, F. Grondin, M. Matallah and A. Loukili, Calculation of the effective viscoelastic properties of the hardening concrete's components, *Coupl. Syst. Mech*., under review, (2017).

[5] J.M. Ricaud and R. Masson, Effective properties of linear viscoelastic heterogeneous media: internal variables formulation and extension to ageing behaviours, *Int. J. Sol. Struc*., **46** (7-8), 1599-1606, (2009).

[6] A. Tran, J. Yvonnet, Q.-C. He, C. Toulemonde and J. Sanahuja, A simple computational homogenization method for structures made of linear heterogeneous viscoelastic materials, *Comp. Meth. Appl. Mech. Eng*., **200** (45-46), 2956-2970, (2011).

DEM calibration procedure for physical bulk tests

S. Ben Turkia*,, P. Pizette*, D.N. Wilke***, N. Govender**** & N. Abriak***

IMT Lille Douai, Institute Mines – Telecom, Douai, France
Arab University of Sciences, Tunis, Tunisia
*** University of Pretoria, Pretoria, South Africa*
**** University of Surrey, Surrey, United Kingdom*
Salma.ben-turkia@imt-lille-douai.fr

For designing and optimizing competitive industrial processes in geotechnics, comminution, powder technology and agronomy, it has become essential to predict the dynamics of granular materials. Unlike a finite element model (FEM), a discrete element model (DEM) allows the properties and effects at particle scale to be directly modelled, which results in significantly different stress fields rather than if they were obtained through macroscopic continuum based models (Bharadwaj & al, 2008). This makes DEM, usually calibrated with merely one or two particle experiments due to high computational costs, a powerful modelling approach. However, the effectiveness of DEM is strongly dependent on identifying an appropriate model, carefully selecting experimental calibration data, and assuring the quality of the calibration process. The two latter aspects of calibration are likely to be the least appreciated and understood in the modelling community and industry. However, when it is done properly, as we hope to show, the results of a DEM approach can faithfully reflect a real process as well as the limitations of DEM. The concerns of identifying whether or not there is sufficient experimental data to conduct sensible calibration will also be addressed.

This study aims to establish a protocol to characterize DEM parameters, within an industrial context, to ensure that the calibrated DEM can be adapted to the needs of industry. First, we address the high computational demands of DEM by considering an experimental approach (DOE) (Box & Draper, 1987) that allows for a massive number of DEM simulations to be conducted in parallel, each with a different set of model parameters. The detailed responses for each DEM simulation are then extracted and used to train a simple feed forward neural network (FFNN), in the form of a radial basis function regressor (RBF) (Hardy, 1971), that predicts the detailed DEM responses for given model parameters without requiring additional DEM simulations. This allows us to consider robust optimization (J.A. Snyman & D.N.Wilke , 2018) to calibrate optimal DEM parameters based on experimental evidence. We leverage the additional power of parallelization to train multiple FFNN to allow different discrete element models to be calibrated. The advantage of this approach is that the FFNN needs to be constructed only once for a given experimental setup and for a specific DEM. This allows the computationally expensive DEM simulations to be completely re-usable. Additionally, by carefully partitioning our experimental data into a calibration set, an interpolation test set and an extrapolation test set, we are able to compare the accuracy (interpolation test set) and generality (extrapolation test set) of various calibrated DEMs. This allows us to choose a sufficiently accurate model that is also general enough to predict responses when conducting simulations that are distinct from the calibration experiment, i.e. the ability of the calibrated DEM to extrapolate away from the calibration experiment. This proposed approach stands in contrast to the often uncoupled DEM parameter calibration or two parameter DEM calibrations often conducted within the context of a non-iterative calibration procedure (Syed & al, 2017).

Specific consideration has been given to the Hertz-Mindlin and spring-dashpot contact model. We chose to calibrate only the coefficient of friction, the coefficient of restitution and the

rolling resistance. Two experimental setups were considered, namely a lab-scale hopper discharge experiment to generate experimental data for our calibration set and an interpolation test set. Secondly, a direct shear test was used to generate experimental data for our extrapolation test set. To demonstrate that the correct model parameters could be obtained, we first solved a problem where the correct model and model parameters – called a virtual problem as shown in Figure 1 – was known. Instead of conducting physical experiments, we simulated experiments by choosing a DEM with known model parameters. We then computed the simulated experimental responses for the hopper discharge and shear box test. Thereafter, a DEM model was characterized from the simulated experimental data to determine whether we could recover the known experimental model parameters. This allowed us to determine whether given experimental data was sufficient or whether the characterization was ill-posed, i.e. when multiple model parameters result in effectively the same DEM response, which indicates insufficient experimental data. This approach was not always robust due to potential overfitting during FFNN construction and parameter calibration, which could effectively conceal the ill-posed nature of a characterization problem.

We therefore extended the FFNN training by adding stochastic noise, 1% and 5% uniform random noise to the DOE simulated DEM responses, so as to make the FFNN more robust when presented with experimental noise data. Stochastic noise could then be added to the simulated experimental data to quantify the sensitivity of the various model parameters, i.e. to quantify the confidence interval of each model parameter. The ill-posedness of this procedure at the individual model parameter level can then be interpreted statistically. In addition, we can now quantify statistically the accuracy and generality of multiple calibrated DEMs by adding stochastic noise to the interpolation and extrapolation test sets.

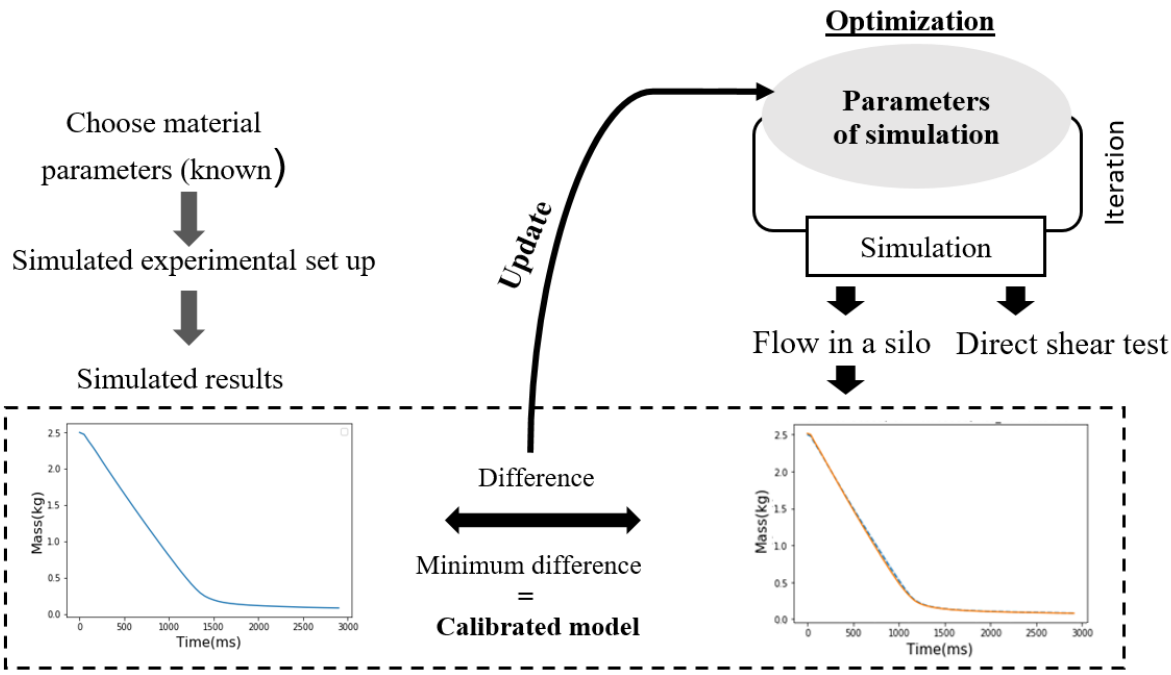

Figure 1. A graphical illustration of the calibration process

References

R. Bharadwaj and al.,2008. A Comparison of Discrete Element Modeling, Finite Element Analysis, and Physical Experiment of Granular Material Systems in a Direct Shear Cell, *AIP Conference Proceedings 969, 221.*

G.E.P. Box and N. R. Draper, 1987. Empirical Model-Building and Response Surfaces, Wiley Series in Probability and Statistics.

R.L. Hardy,1971. Multiquadric Equations of Topography and Other Irregular Surfaces, *Journal of Geophysical Research, vol. 76, pp. 1905–1915.*

J.A. Snyman and D.N.Wilke,2018. Practical mathematical optimization*, Springer Optimization and Its Applications 133.*

Z. Syed and al ,2017. "A coupled sliding and rolling friction model for DEM calibration," *Journal of Terramechanics*, vol. 72, pp. 9–20.

On the stabilizing role played by rattlers in granular materials

A. Wautier[1,2,3], S. Bonelli[2] & F. Nicot[3]
[1]AgroParisTech-ENGREF, 19 avenue du Maine, 75732 Paris, France.
[2] Irstea UR RECOVER, 3275 Rte Cézanne, CS 40061, 13182 Aix-en-Provence Cedex 5, France.
[3]Université Grenoble Alpes, Irstea, UR ETGR, 2 rue de la Papeterie BP 76, F-38402 St-Martin-d'Hères, France.
antoine.wautier@irstea.fr

For frictional granular materials such as soils or rocks, it is now well established that the normality of the flow rule as proposed by Drucker and Prager (1952) does not hold, and that the plastic behaviour is non-associated. The non-associated character of the flow rule imposes the tangent constitutive tensor not to respect the so-called major symmetry (Darve and Laouafa, 2000). Therefore, the tangent elasto-plastic matrix linking incremental stress and strain (in vector notations) is no longer symmetric (Griffiths and Willson, 1986) which makes it possible to observe instabilities in granular materials before the plastic limit surface is reached, provided that materials are loaded along "wedge paths" (Li and Richmond, 1997; Li and Karr, 2009). Such critical loading path is illustrated in Figure 1 below.

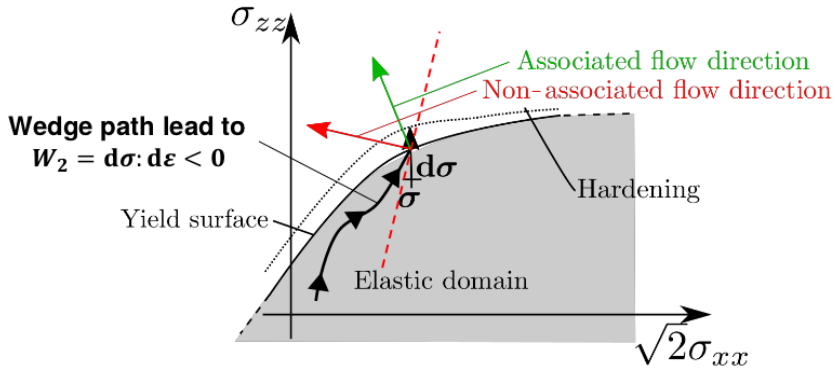

Figure 2: Illustration of the existence of material instability in non-associated materials loaded along a wedge path.

If analyses are limited to divergence instabilities, the second-order work criterion as introduced by Hill (1958) will provide an energy interpretation for the occurrence of such instabilities. For a monotonous increase loading, it is the first instability criterion to be encountered (Challamel et al., 2010), whereas other instability criteria are simply specific cases associated with specific failure mechanisms.
The aim of this proceeding (based on Wautier et al., 2018) is to highlight the relation between plastic deformation and mechanical instability in granular materials and to exhibit the particular role played by the rattlers (i.e., particles with no contacts in the absence of gravity forces) with respect to the development of plastic strain and instability. The results presented are of particular interest with respect to the internal erosion phenomenon for which the finest particles of a soil may be extracted under the action of an internal fluid flow.

1. Non-associated plasticity and mechanical stability

Thanks to the use of the YADE software, a cubic assembly of 10,000 spherical particles was generated following a uniformly distributed particle size distribution with $r_{max} = 3.5\, r_{min}$.

At the microscale, the interactions between grains are modelled according to a classical elasto-frictional contact law with parameters given in Table below.

Parameters	Value
Density	3,000 kg.m-3
Young Modulus (E)	356 MPa
Stiffness ratio (ν)	0.42
Inter-particle friction angle (φ)	35°
Particle-wall friction angle	0°
Number of particles	10,000

A loose sample with a void ratio of 0.73 was prepared subjected to a drained triaxial under a confining pressure of 100 kPa. For a particular stress state i) identified as unstable in the sense of the second order work criterion and ii) characterized by a stress ratio $\eta = {}^{q}/_{p} = 0.45$, a non-associated elasto-plastic model was fitted to describe the incremental response of the material in the Rendulic plane of axisymmetry. This model relies on the 6 fitted parameters highlighted in red in Figure 2 whose numerical values are given in the following Table.

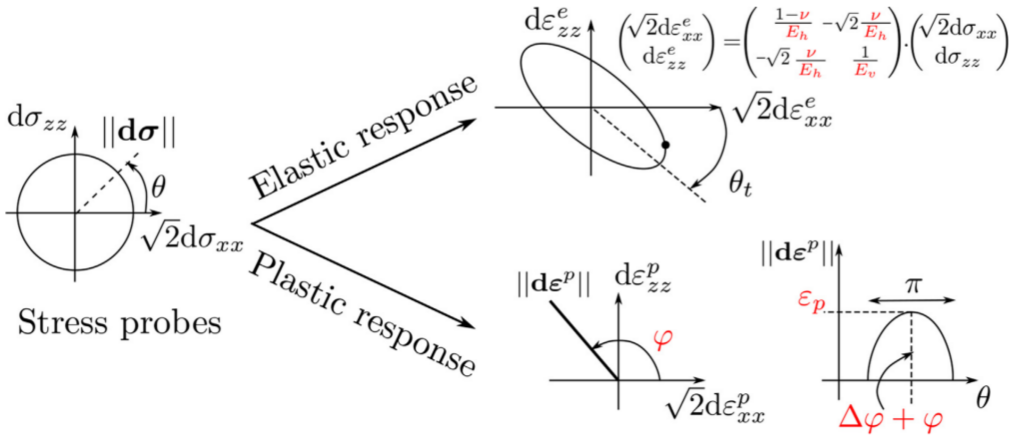

Figure 3: Non-associated elastoplastic fitted response in the incremental strain space corresponding to stress probes describing a circle in the Rendulic plane. The strain response has been broken down into an elastic part characterized by three parameters and a plastic part described with three parameters.

Elastic behaviour	Plastic behavior
$E_h = 25.2$ **MPa**	$\varphi = 113.8°$
$E_v = 32.5$ **MPa**	$\Delta\varphi = 25.9°$
$\nu = 0.31$	$\varepsilon_p = 4.69\ 10^{-2}$

The fitted phenomenological model is shown to account very well for the second-order work circular envelope computed in the Rendulic plane, while the magnitude of the plastic intensity ε_p is shown to control the existence and the width of the cone of instability characterizing unstable materials in the sense of the second-order work criterion.

2. A conjecture on the stabilizing role played by rattlers

Despite their non-contribution to stress transmission in granular materials, the following two schematic diagrams illustrate the two impacts of the rattlers on the incremental plastic behaviour in granular materials.

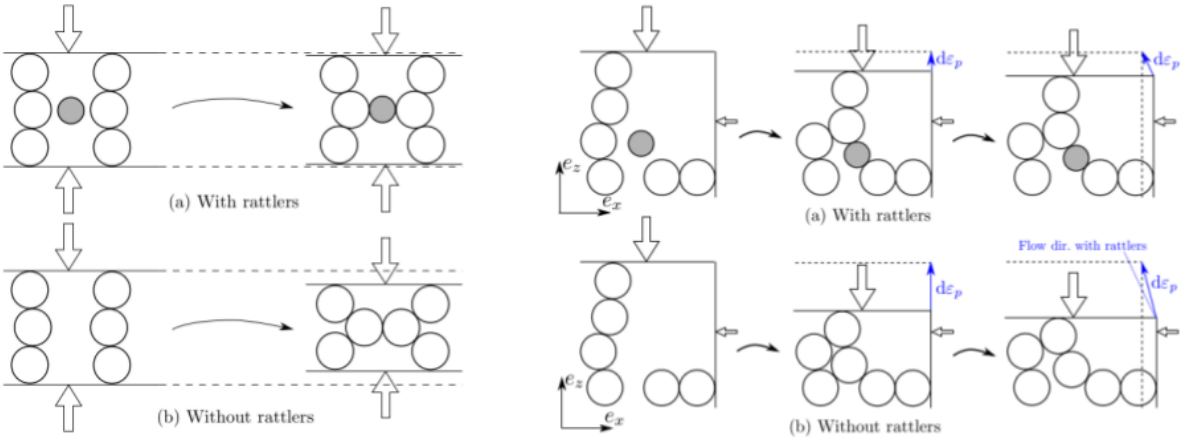

Figure 4: Impact of rattlers on the plastic flow rule: flow intensity (left) and plastic flow direction (right).

- By facilitating the creation of new force chains, if the existing ones failed to withstand an incremental load, the rattlers control the development of incremental plastic strain. As a result, the rattlers can limit the plastic strain intensity ε_p and thus contribute to ensuring mechanical stability.
- For an anisotropic stress state, force chains are mainly oriented in the vertical direction. As a result, should the force chain collapse, the incremental strain would develop mainly in the vertical direction. The control exerted by the rattlers on the development of the incremental plastic strain is thus more important in the direction parallel to the force chains than in the transverse direction. This explain why the rattlers control the non-associated plastic flow direction φ .

3. DEM assessment of rattlers contributing to plasticity and stability

The conjecture formulated in the previous section can be tested numerically in DEM simulations by removing or adding rattlers in the sample prepared in the stress state $\eta = 0.45$ (section I).

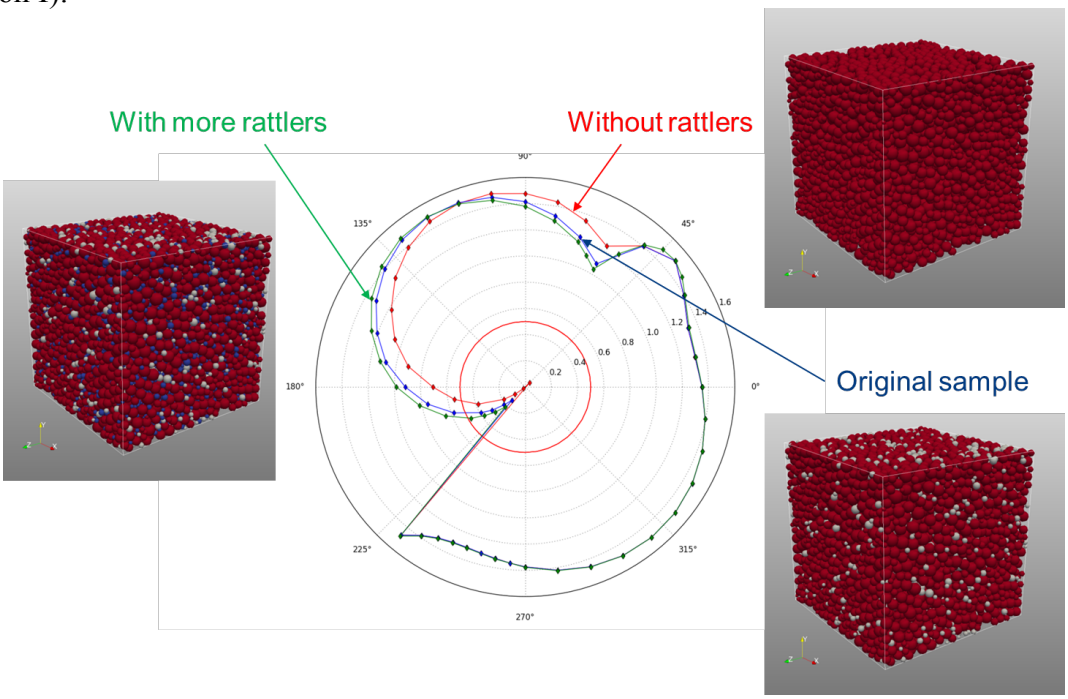

Figure 5: Circular envelopes of second order work plotted in the Rendulic plane for stress controlled directional analyses. Three microstructures have been considered.

The results of these two artificial microstructure modifications are shown in Figure 4. In both cases, the modified samples are still identified as unstable (a cone of instability is observed for $\theta \sim 225°$), but the width of the cone is increased by removing rattlers and vice versa, which illustrates the stabilizing role played by rattlers.

By modifying merely the two plastic parameters ε_p and φ of the phenomenological model fitted for the original microstructure, it is possible to describe accurately the two circular envelopes of Figure 4 corresponding to the addition or removal of rattlers. This is illustrated in Figure 5.

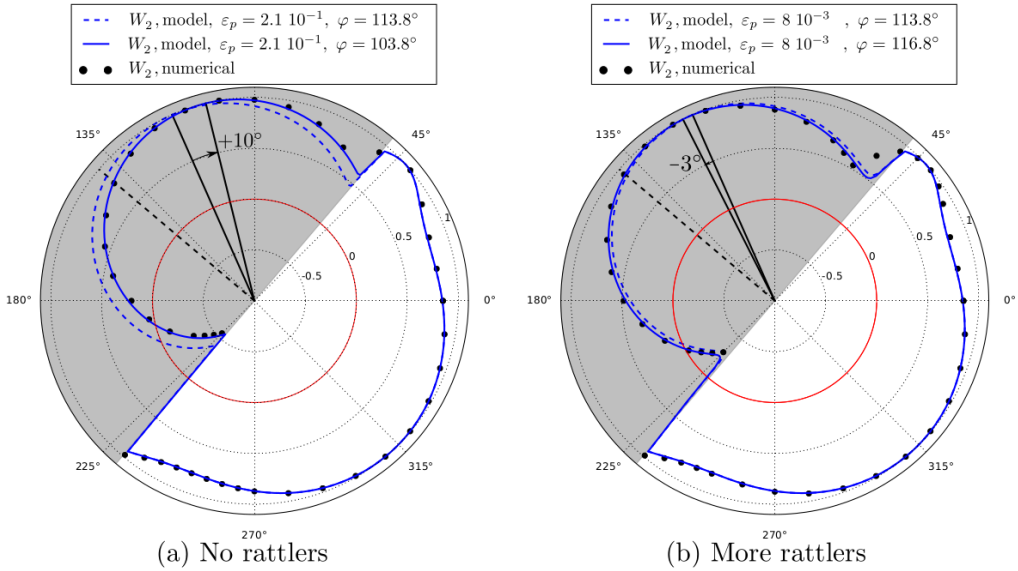

(a) No rattlers (b) More rattlers

Figure 6: Updated second-order work (W_2) envelopes accounting for the two modified microstructures. The blue dashed lines correspond to an update in ε_p alone. The blue solid line correspond to an update in both ε_p and φ.

If only the plastic intensity (ε_p) is updated, the circular envelopes corresponding to the two modified microstructure will not be well described. But if the plastic flow direction (φ) is also updated, then the updated phenomenological model will be able to account very well for the microstructure modifications. This confirms numerically the two conjectures illustrated in Figure 3.

References

Challamel, N., Nicot, F., Lerbet, J., Darve, F., 2010. Stability of non-conservative elastic structures under additional kinematics constraints. *Eng. Struct.* 32 (10), 3086–3092.

Darve, F., Laouafa, F., 2000. Instabilities in granular materials and application to landslides. *Mech. Cohesive-Frict. Mater.* 5 (8), 627–652.

Drucker, D.C., Prager, W., 1952. Soil mechanics and plastic analysis or limit design. *Q. Appl. Math.* 10 (2), 157–165.

Griffiths, D., Willson, S., 1986. An explicit form of the plastic matrix for a mohr–coulomb material. *Int. J. Numer. Meth. Biomed. Eng.* 2 (5), 523–529.

Hill, R., 1958. A general theory of uniqueness and stability in elastic-plastic solids. *J. Mech. Phys. Solid.* 6 (3), 236–249.

Li, M., Richmond, O., 1997. Intrinsic instability and nonuniformity of plastic deformation. *Int. J. Plast.* 13 (8–9), 765–784.

Li, Y., Karr, D.G., 2009. Prediction of ductile fracture in tension by bifurcation, localization, and imperfection analyses. *Int. J. Plast.* 25 (6), 1128–1153.

Wautier, A., Bonelli, S., & Nicot, F., 2018. Rattlers' contribution to granular plasticity and mechanical stability. *Int. J. Plast.* In press.

Multiscale modelling of cohesive granular materials: possible ways to extend the 3D H-model

M. Miot[(1)(2)] & G. Veylon[(1)], F. Nicot[(3)] & P. Philippe[(1)]

[(1)]IRSTEA UR RECOVER, Aix-en-Provence
[(2)]Aix-Marseille Université
[(3)]IRSTEA UR ETGR, Grenoble
marie.miot@irstea.fr

Microdirectional models which incorporate a mesoscopic scale constitute a powerful alternative to continuous models, defined at the macroscopic scale on phenomenological bases, and discrete models which are less adaptable to structure-scale analysis. The 3D H-model (Xiong, 2017) introduces a mesoscale between the representative elementary volume and the contact between grains. The granular assembly is modelled as a spatial distribution of ten-grain cells (Figure 1). The incremental constitutive relationship is obtained by considering the equilibrium of each grain within its cell and, then, by stress averaging over all the grain cells. At the mesoscopic scale, the cells are supposed to have three planes of symmetry. The geometry of each cell is consequently fully characterized with merely the grain interpenetrations and the opening angle α (Figure 1).

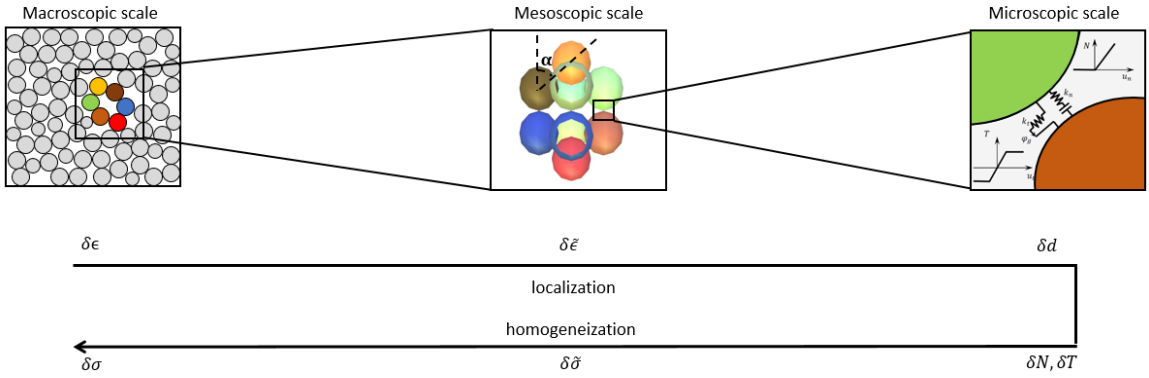

Figure 1. Multiscale concept of the H-microdirectional model

The original 3D H-model was developed for purely frictional materials. The purpose of the present work is to analyze the influence of solid and liquid bridges at the mesoscopic scale. The impact of the solid and liquid cohesion on the behavior of an axially oriented cell with an initial opening angle of 55° is evaluated along a drained triaxial loading within the Discrete Element Method (DEM) based software YADE (Smilauer *et al.*, 2015).
The presence of solid bridges is modelled by introducing normal and tangential cohesion into the grain contact law implemented in YADE (Smilauer, 2010). It is shown that the normal cohesion Cn increases the vertical peak stress and the corresponding strain (Figure 2). Interestingly enough is that, for large strains (after solid bridge failure), there is a convergence between the stress state for a non-cohesive cell and the stress state for a cohesive cell. It has also been shown that the shear cohesion Cs has no impact on the response of the cell during this loading.

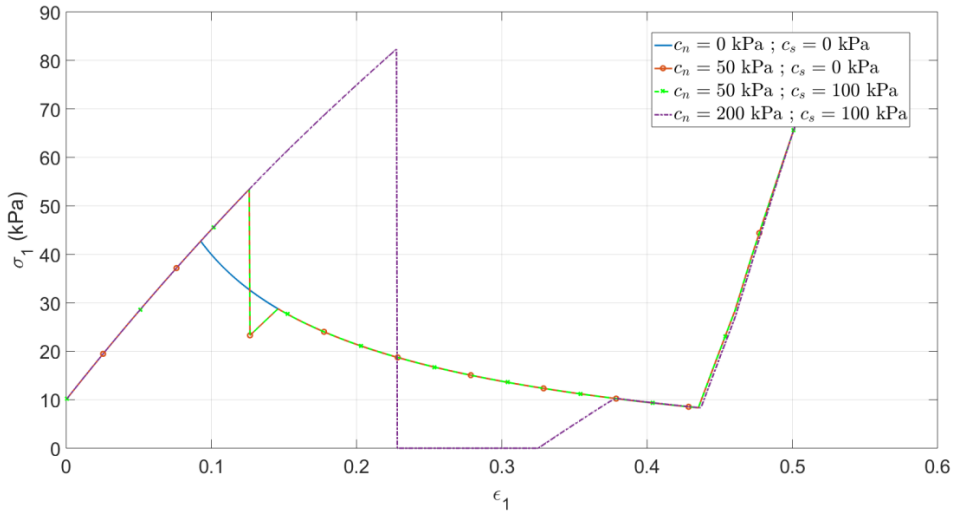

Figure 2. Axial stress for several cohesion cases as a function of the axial strain during a deviatoric loading

It has been verified that introducing liquid bridges (related pendular regime, already implemented in YADE (Duriez &Wan, 2016) does not change the response of the grain-cell. Further research will study the influence of the grain-cell saturation degree on the stress state of the grain-cell in funicular and capillary regimes. This work is currently performed with the surface minimizer software Surface Evolver (Figure 3).

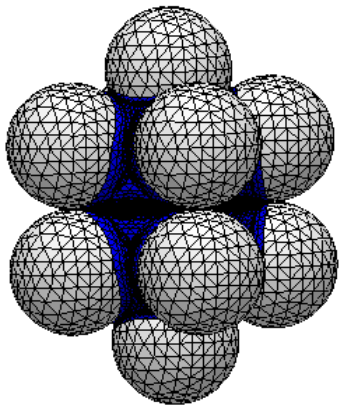

Figure 3. Water cluster in a hexagonal cell modelled with Surface Evolver

References

Duriez, J. and Wan, R**.,** 2017. Contact angle mechanical influence in wet granular soils. *Acta Geotechnica,* 12, pp 67-83

Smilauer, V., 2010. Cohesive particle model using the discrete element method on the Yade platform. *Czech Technical University in Prague; Université de Grenoble.*

Smilauer, V., Catalano, E., Chareyre, B., Dorofeenko, S., Duriez, J., Dyck, N. … Yuan, C., 2015. Reference Manual. http://doi.org/10.5281/zenodo.34045

Xiong, H., 2017. Multiscale modelling of granular materials in application to geotechnical engineering problems. *Université Grenoble Alpes.*

A Halo based approach to better control the stress field dispersion in 3D Discrete Elements Method simulation

D. Moukadiri*, W. Leclerc*, M. Guessasma*, E. Bellenger* & F. Druesne**

**Université de Picardie Jules Verne, LTI, EA 3899 MIM. 48 Rue d'Ostende, 02100 Saint-Quentin*

***Université de Technologie de Compiègne, Roberval, CNRS FRE 2012. Centre de Recherche de Royallieu CS 60319 - 60203 Compiègne Cedex*

dounia.moukadiri@u-picardie.fr

Despite the multiple advantages of agrocomposite in terms of lightness and compliance with environmental standards, the variability in the mechanical performances at the end of the manufacturing process impedes their mass production and makes them less competitive compared to conventional materials. The objective of the VARIATION project, funded by the region Hauts-de-France and the FEDER, is to promote the mass production of composites reinforced by natural fiber and to control their performance at the macroscopic scale. Considering the multiscale effect and the discontinuities that arise in agrocomposite simulation, we have used the Discrete Element Method (DEM) (Leclerc, 2017), based on the cohesive beam model (Figure 1), which is a good alternative to classical continuous methods such as the Finite Element Method (FEM). The latter loses its effectiveness in modelling cracking and complex microstructures such as composite materials, whereas DEM naturally takes into account discontinuities. However, in DEM simulation the stress field is locally distracted, which leads to a heterogeneous field, even in the case where this latter is theoretically homogeneous. As a result, the process to initiate cracking is systematically accelerated.

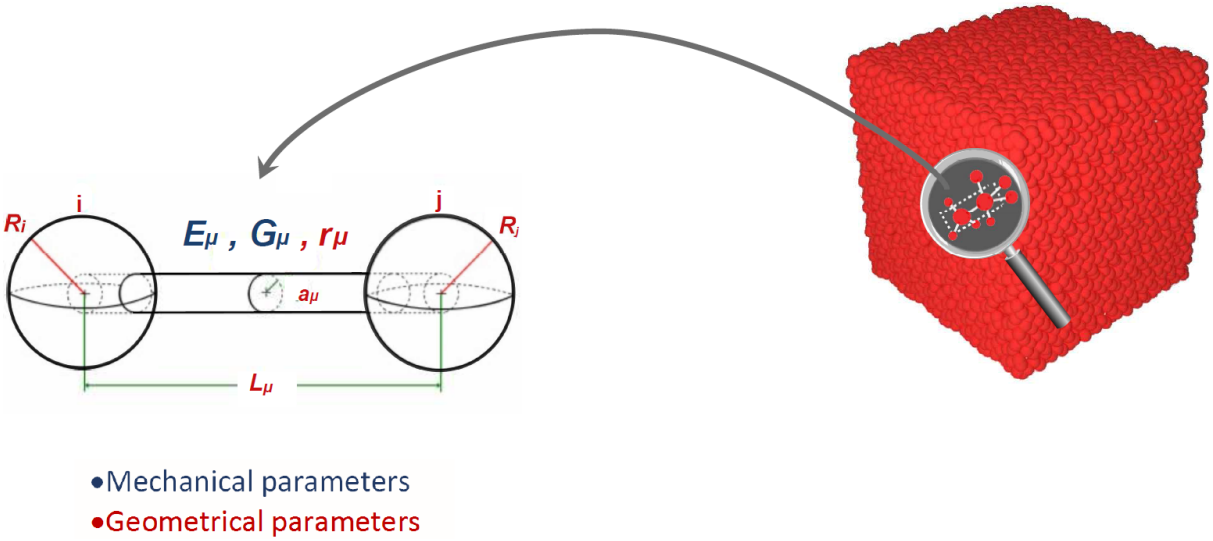

Figure 1. Cohesive beam model

To resolve this problem, we have introduced a mesoscale using an approach called Halo. The aim of this approach is to better control the level of the stress field dispersion. The main idea is to evaluate the stress at the scale of the discrete element (DE) taking into consideration the effects of DEs located in its neighborhood, inside what we name Halo of the DE (Figure 2). The stress field is obtained through a Love-Weber formulation (Love, 1927) (Weber, 1966).

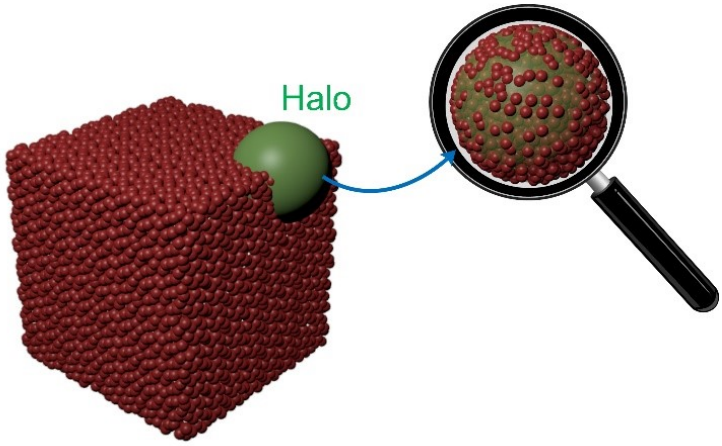

Figure 2. Example of a Halo introduced at the mesoscopic scale

The size of the halo has been directly related to the expected state of dispersion and has been discussed in the case of both the homogeneous and the heterogeneous medium. Comparison with FEM has been done. Results show a good agreement between the two approaches using 1770 DEs per Halo (Figure 3). The Halo approach is well adapted to control the stress dispersion regardless of the geometry of the inclusion (cylindrical or spherical). However, it should be noted that the size of the Halo has to be carefully chosen to smooth out the stress field sufficiently but not excessively so that no information should be lost where local stress gradients may arise. We expect to develop the Halo approach in order to take into consideration stress concentrations and gradients.

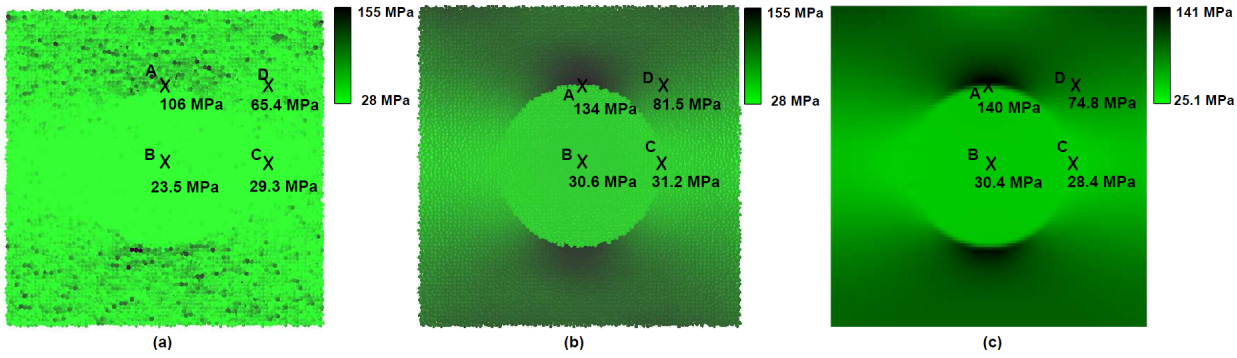

Figure 3. Snapshots of stress field in a pattern with cylindrical inclusion: case of CDEM with 2 (a) and 1770 (b) DEs per Halo and case of FEM using 5 million tetrahedra (c) (cutting plan y=L/2)

As a next step, we intend to implement a numerical approach to take into consideration the variability of the input parameters at the microscopic scale and to estimate the transfer of

variabilities to the macroscopic one, using the Certain Generalized Stresses Method formulation (Lardeur and al., 2012) (Yin and al., 2016).

References

Lardeur, P., Arnoult, E., Martini, L. and Knopf-Lenoir, C., 2012. The certain generalized stresses method for the static finite element analysis of bar and beam trusses with variability. *Finite Elements in Analysis and Design, 50*, pp. 231-242.

Leclerc, W., 2017. Discrete element method to simulate the elastic behavior of 3d heterogeneous continuous media. *International Journal of Solids and Structures*,121, pp. 86-102.

Love, A., 1927. A treatise of mathematical theory of elasticity. *Cambridge University Presse, Cambridge.*

Weber, J., 1966. Recherches concernant les contraintes intergranulaires dans les milieux pulvérulents, application la rhéologie de ces milieux. *Bulletin de Liaison des Ponts et Chaussées.*

Yin, Q., Druesne, F. and Lardeur, P., 2016. The CGSM for static analysis of multi-layered composite plates with variability of material and physical properties. *Composite Structures*, 140, pp. 360-368.

Creep behaviour of an overconsolidated clay in relation to the microstructure

Dan Zhao *, Mahdia Hattab, Zhenyu Yin***, Pierre-Yves Hicher******

**Zhejiang University of Water Resources and Electric Power, Hangzhou, China*
*** LEM3, UMR CNRS 7239, Unversité de Lorraine, France*
**** CEE, The Hong Kong Polytechnic University, Hong Kong, China*
***** GeM, UMR CNRS 6183, Ecole Centrale de Nantes, France*
zhaodan1120@gmail.com

Abstract: The aim of this study is to analyse the creep behaviour of a typical clay from triaxial tests as well as to understand the microstructural mechanisms of this behaviour. The macroscopic results obtained showed that both dilatancy and contractancy could occur during creep. At the microscopic scale, the results indicate that the microstructural evolution of the clay along mechanical loading is dependent on the stress history. The creep dilatancy at the macroscopic level is related to the expansion of micro pores and micro cracks within overconsolidated samples.

Introduction

It is generally accepted that under drained triaxial loading on saturated clays, normally consolidated and lightly overconsolidated clays exhibit a contractant behaviour, whereas heavily overconsolidated clays exhibit a dilatant behaviour. Tavenas et al. (1978) performed drained triaxial creep tests on lightly overconsolidated clay along different stress paths. The authors observed a contractive creep, a tiny volume change and an obvious dilatancy under an increasing, a constant and a reduced p' stress path, respectively. During creep, the overconsolidation condition is not the only factor that influences the contractancy/dilatancy creep behaviour; the stress path or the stress state before the creep phase should also be considered. At the microscopic scale, the presence of clay particles is one of the main reasons for soil creep deformation. According to Akagi (1994) the consolidation is based on the drainage of pore fluids and the deformation of pores. At present, the study on the microscopic mechanism of creep for soft clay is still in its infancy due to the limitations of experimental technique and a lack of experimental data.

In this paper, triaxial creep tests have been conducted on normally consolidated and overconsolidated saturated reconstituted clay. After creep, the microstructure of the triaxial samples were analysed with the scanning electron microscope (SEM). The time-dependent characteristics of the volumetric creep strains, after a purely deviatoric stress loading, are discussed. The evolution of soil particles and micro pores after creep has also been studied.

Material and experimental testing

The soil selected for the research is an industrial clay named Kaolinite K13, the liquid limit is 42% and the plastic limit is 19%. The dried clay powder was mixed with de-aired water; the slurry was preconsolidated afterwards for at least 3 weeks. The soil was then cut into cylindrical specimen of 75 mm in height and 50 mm in diameter for triaxial testing.

After having been isotropically consolidated to a certain OCR (OCR=1, 1.5, 2.5 and 4), the triaxial specimen were loaded up to a given stress level under constant p' stress path, during which the volumetric strain was created by the sole deviatoric stress q (Hattab & Hicher, 2004). Then the stress state was maintained constant within 7 to 10 days so that the creep

deformation could be observed. Small samples were cut from the core zone of the triaxial specimens after creep. The region of interest for observation is the surface of the vertical plane parallel to the vertical stress σ'_1.

Results and discussion

Macroscopic scale. Figure 1 presents the results of 6 tests during the constant p' stress path. It can be seen from Figure 1a that for the normally consolidated sample, contractancy was detected from the beginning of the loading. For the lightly overconsolidated samples, a very small volumetric strain was obtained. As for the highly overconsolidated sample (OCR=4), a slight dilatancy was observed at the beginning of the loading, which was followed by a clear dilatancy. The results obtained here are in agreement with those obtained by Hattab and Hicher (2004) on the same constant p' triaxial tests. Thereafter, the three volumetric strain domains identified by Hattab and Hicher, contractancy, no-volume change and dilatancy, were introduced into this research (Figure 1b).

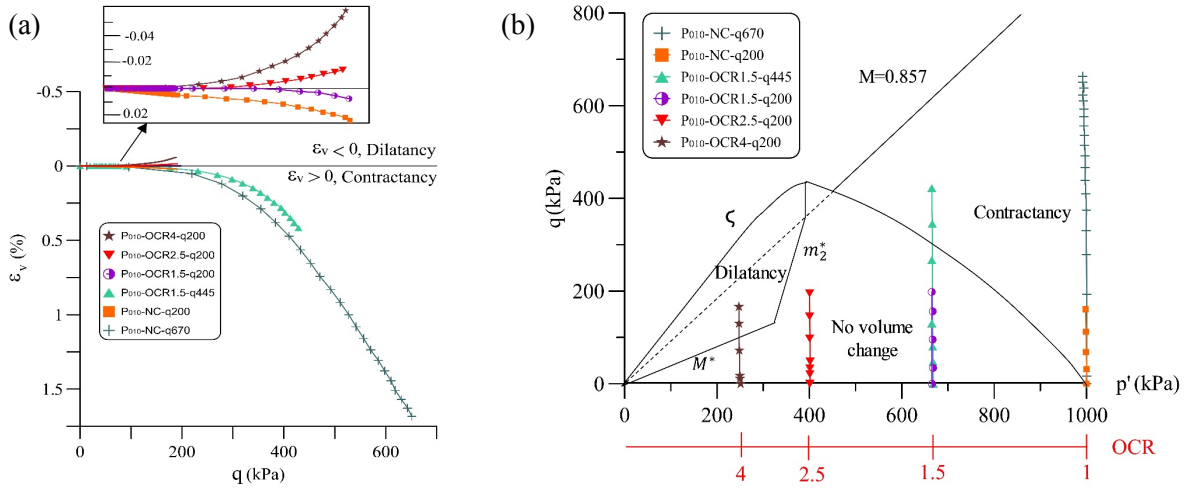

Figure 1. Mechanical behaviour on constant p' stress path (a) ε_v - q plane (b) p'- q plane

Figure 2 presents the results of the creep tests performed after the constant p' stress paths. It can be seen that in the contractancy domain for the normally consolidated samples (P_{010}-NC-q667 and q200) and the lightly overconsolidated sample (P_{010}-OCR1.5-q445), a contractive behaviour was obtained (Figure 2a). The results of the creep phase suggested that the deformation tendency was the same as the one obtained under constant p' loading. In the dilatancy domain for the highly overconsolidated sample (P_{010}-OCR4-q200 in Figure 2b), an obvious dilatancy was detected from the start of the pure creep phase. As for lightly overconsolidated specimens in the no-volume change domain (P_{010}-OCR1.5 and 2.5-q200 in Figure 2b), the results showed a volumetric strain evolution alternating between very small contractancy/dilatancy or dilatancy/contractancy. After the constant p' stress path, it appears that the volumetric domain, in which the creep test is conducted, governs the development of the volumetric creep strain.

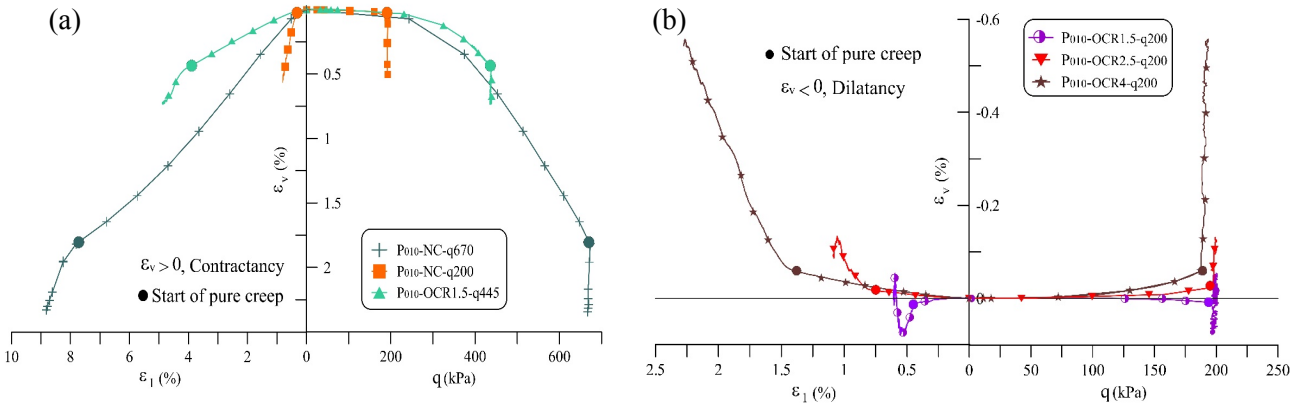

Figure 2. Evolution of strains (a) in the contractancy domain (b) in the no-volume and dilatancy domains

Microscopic scale. In order to see more clearly the microstructure evolution during creep, we performed 6 shear tests along exactly the same stress path and stress level as in the creep tests. Figure 3 presents the representative SEM photos of tests P_{010}-NC-q200 in the contractancy domain after shear and after creep. Generally, the particles are face-face associations shown by the thin layers in the side view of SEM photos. Furthermore, it appears that the soil particles tend to be more oriented after a period of creep time (Figure 3b) rather than after shear (Figure 3a).

The representative SEM images in Figure 4 shows the structural evolution of highly overconsolidated samples. The photos show the appearance of a structural isotropy tendency which develops from dilatancy in the creep phase. Locally we observe groups of particle arrangement (red dotted line in Figure 4b) forming random open micro-cracks inside the material (blue circles in Figure 4b). Unlike the samples in the contractancy domain, weaker preferential orientations are identified for samples in the dilatancy domain.

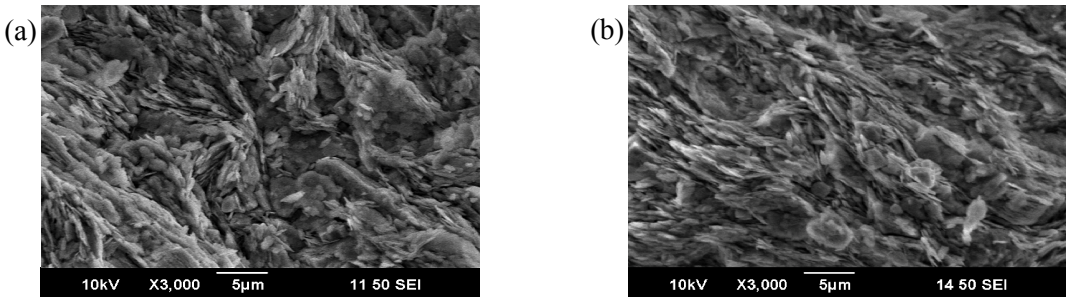

Figure 3. Microfabric of tests P_{010}-NC-q200 in the contractancy domain (a) after shear (b) after creep

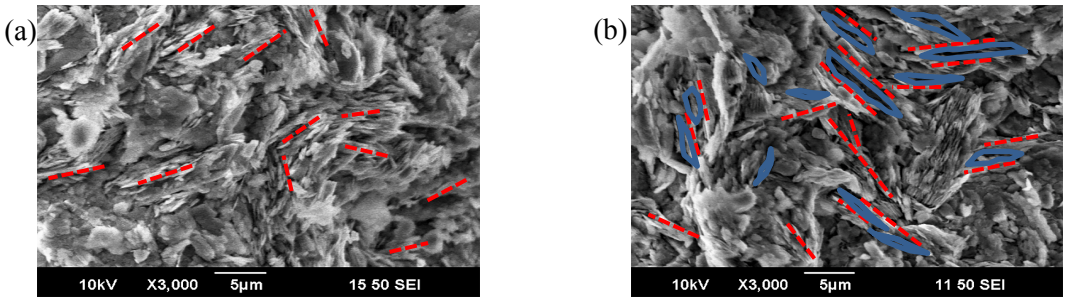

Figure 4. Microfabric of tests P_{010}-OCR4-q200 in dilatancy domain (a) after shear (b) after creep

Summary

(1) In the contractancy domain for normally consolidated samples: creep contractancy was obtained for any stress level. Generally the particles orient themselves parallel to each other. Structural anisotropy increases with creep contractancy.

(2) In the dilatancy domain, creep dilatancy was clearly observed for the highly overconsolidated samples. Structural isotropy formed at the end of monotonic loading. This structural isotropy continues to develop during creep, formed by groups of random particles. The expansion of micropores results in the opening up of microcracks inside the material that contributes to the dilation at the scale of the sample.

(3) In the no-volume change domain for the lightly overconsolidated specimens, alternating small contractancy/dilatancy amplitudes appeared during the creep stage. In this domain, no volumetric strain change can be assumed during creep.

References

Akagi, H. (1994). A physico-chemical approach to the consolidation mechanism of soft clays. *Soils and Foundations*, 34(4), 43-50.

Hattab M, Hicher PY (2004) Dilating behavior of overconsolidated clay. *Soils and Foundations* 44(4): 27–40.

Tavenas F, Leroueil S, La Rochelle P, Roy M (1978) Creep behaviour of an undisturbed lightly overconsolidated clay. *Can Geotech J.*, 15(3):402–423.

Initiation and propagation of crack in clayey materials in a bending test related to initial suction

L. Ighil Ameur*, M. Jrad & M. Hattab****

CEREMA NC
*** LEM3, UMR CNRS 7239, Unversité de Lorraine, France*
mohamad.jrad@univ-lorraine.fr

Introduction

The presence of cracks affects the clay concrete structure. The drying phenomenon, which causes suction to develop in the material, appears to be one of the reasons for the cracking of clays. During drying, Wei et al. (2016) showed that the initiation and propagation of cracks are due to different mechanisms; one of these being the cracking induced by tensile stresses.
Many researchers have focused on the importance of the tensile strength, among of them: Bishop and Garga (1969), Ajaz and Parry (1975), Tang and Graham (2000); or, more recently, Thusyanthan et al. (2015). The tensile cracking seems to occur when induced tensile stress exceeds tensile strength. Ajaz and Parry (1975) and Thusyanthan et al. (2007) used the results of the beam flexion test. The results show that the failure tensile strain increases as water content increases.
In this work, we have mainly focused on the characterization and the understanding of the tensile strength properties of clayey soils as well as their relationships with initiation and propagation of tensile cracks using an indirect tensile test apparatus by bending. Results are analysed with the DIC methods.

Experimental tests and results

The clayey soil used in this study was Kaolinite K13. The specimen preparation method was the following: first, the hydrated clay powder was consolidated under a vertical stress of 120 kPa. The preconsolidated specimen was then cut into small beam samples of 35 mmX10 mmX10. The samples of small-beams were submitted to three different levels of suction (361 MPa, 110 MPa and 38 MPa) in a vacuum desiccator with salt solutions (Fleureau et al. 1993).
During the test, the sample was loaded until breakage. The test apparatus developed by Ighil Ameur (2016) is equipped with a force sensor and a comparator to capture force and displacement. The sample was loaded at a rate of 10−3 mm/min. For every stored force value, the images were simultaneously captured by a camera for DIC analyses. From the results obtained, force versus displacement, we notice that the bend strength corresponding to the maximum force is influenced by the suction. Bend strength clearly increases with the increase of suction (Ighil Ameur and Hattab 2017).
The evolution of strain can be shown through the full field longitudinal strain maps presented in Figure 1. At the peak of force (image i), the maximum and the minimum ε_{xx} are equal to +0.2% and −0.096%, respectively. The tension zone of the beam is shown in red, where the average ε_{xx} is equal to +0.2%. This stage defined crack initiation as visible in the image. Then, when the bend force decreases, the corresponding DIC (image i + 1) shows the propagation of the crack and the extension increasing up to +6.3%. At the end of the test (image f), the directions of the displacement vectors (white vectors) indicating the opening mechanism of the crack can be clearly observed.

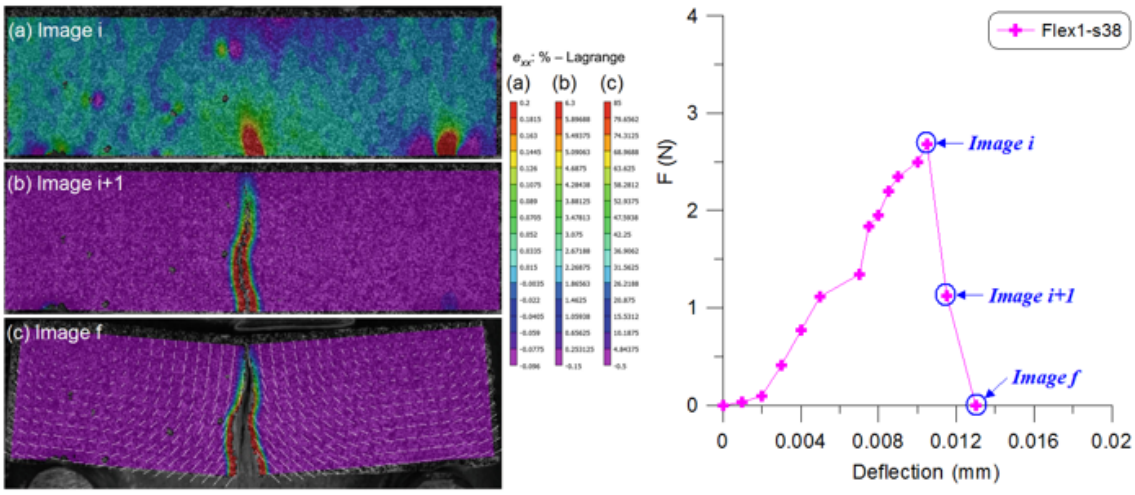

Figure1. Longitudinal local strain ε_{xx} at (a) image i; (b) image i + 1; (c) image f and their positions on tensile stress curve.

References

1- Bishop AW, Garga VK (1969) Drained tension tests on London Clay. *Géotechnique* 19:303–313

2- Ajaz A, Parry RHG (1975a) Stress-strain behaviour of two compacted clays in tension and compression. *Géotechnique* 25(3):495–512

3- Ajaz A, Parry RHG (1975b) Analysis of bending stresses in soil beams. *Géotechnique* 25(3):586–591

4- Fleureau JM, Kheirbek-Saoud S, Soemitro R, Taibi S (1993) Behaviour of clayey soils on drying-wetting paths. *Can Geotech J.* 30(2):287–296

5- Tang GX, Graham J (2000) A method for testing tensile strength in unsaturated soils. *Geotech Testing J*. 23(3):377–381

6- Thusyanthan N. I., Take W. A., Madabhushi S. P. G., and Bolton M. D. (2007) Crack initiation in clay observed in beam bending. *Géotechnique* 57 (7): 581-594

7- Wei X, Hattab M, Bompard P, Fleureau JM (2016) Highlighting some mechanisms of crack formation and propagation in clays on drying path. *Géotechnique* 66(4):287–300

8- Ighil Ameur L. (2016) Étude expérimentale du phénomène de l'endommagement et de la fissuration d'une matrice poreuse. *Doctoral dissertation*, Université de Lorraine, France

9- Ighil Ameur L., Hattab M. (2017) Crack Initiation and Propagation of Clays Under Indirect Tensile Strength Test by Bending Related to the Initial Suction. In: Ferrari A., Laloui L. (eds) *Advances in Laboratory Testing and Modelling of Soils and Shales* (ATMSS). ATMSS 2017. Springer Series in Geomechanics and Geoengineering. Springer, Cham

Discrete modelling for civil engineering applications: contribution from the High Performance Computing (HPC)

Patrick Pizette*, Nicolin Govender*,, Daniel Wilke***, Nor-edine Abriak***

**IMT Lille Douai, Univ. Lille, EA 4515 - LGCgE - Laboratoire de Génie Civil et géoEnvironnement, départment Génie Civil & Environnemental, F-59000 Lille, France*
*** Department of Chemical Engineering, University of Surrey, United Kingdom*
****Center of Asset and Integrity Management, University of Pretoria, South Africa*
Email: patrick.pizette@imt-lille-douai.fr

Granular material processing is crucial to a number of industries such as pharmaceuticals, construction, mining, geology and primary utilities. The handling and processing of granular materials represents roughly 10% of annual energy consumption (Duran, 2012). In the US alone, energy requirements across Coal, Metal and Mineral Mining amounted to 1246 Tbtu/yr in 2007, whereas the practical minimum energy consumption is estimated to be 579 Tbtu/yr (Mining, 2007).

The Discrete Element Method (DEM) proposed by Cundall and Strack (Cundall & Strack, 1979) for geotechnical applications has matured to the point that numerous and diverse industrial civil engineering applications are now being considered for the first time. The limiting factor has been the limited number of particles that can be practically considered for industrial applications. Even if numerous assumptions have been made to enable particle shapes to be reduced to spheres, the concurrent processing limitations of the CPU have nevertheless hindered advancing the DEM for practical purposes.

Recent developments for simulating Discrete Element Models on Graphical Processor Unit (GPU) hardware have brought new perspectives to practical industrial granular applications. In particular, Govender et al. (Govender & al, 2016) have simulated industrial processes that include ball mill simulations and hopper discharge using 16 million particles on a single portable computer which allows new computational performance levels to be achieved.

In collaborative studies between IMT Lille Douai (France), CSIR (South Africa) and the University of Pretoria (South Africa) started in 2015, the GPU based DEM simulations have been extensively validated for silo discharge and milling simulations using both spherical and polyhedral shaped particles (Govender et al. 2015, Pizette et al. 2017 and Govender et al. 2018). These studies have clearly demonstrated that GPU-based DEM to model complex particle shapes in a reasonable computational time for sufficiently large number of particles are valid for practical purposes. These studies proposed a systematic comparison between DEM–GPU simulations and experiments for idealized particles (convex polyedral or non-convex polyhedral particles (Wilke et al. 2017)). This allows for systematic validation of developed GPU codes as the complexity of particles increases.

In this presentation, we show via several applications in civil engineering the contribution and the potential of the GPU to tackle large scale industrial cases via DEM simulations. The focus of our attention is specifically directed to the newly developed BlazeDEM3D-GPU framework (BlazeDEM3D-GPU) for an industrial flow investigation (Civil Engineering). Consider Figure 1, where we simulate the granular flows on storage silos of an industrial concrete facility located in France with diameter 8 m and height 17 m. DEM simulations were performed to investigate the influence of particle sizes (equivalent size for the 20/40-mesh gravel) and inter-particle cohesion on the bulk flow rate and induced shear stress for a number

hopper shapes. Hoppers are composed of the assembly of two coaxial conical shapes with different discharge angles and different cylindrical extensions between the two cones. The preliminary results indicate that the shape of the hopper influences significantly the discharge rates for the same material parameters.

To conclude, as required for an industrially relevant application, up to ten million particles were simulated with DEM within a practically accepted time frame (30 – 60 millions of particles). This study highlights that large scale DEM simulations can be performed within a reasonable time frame when the GPU is utilized.

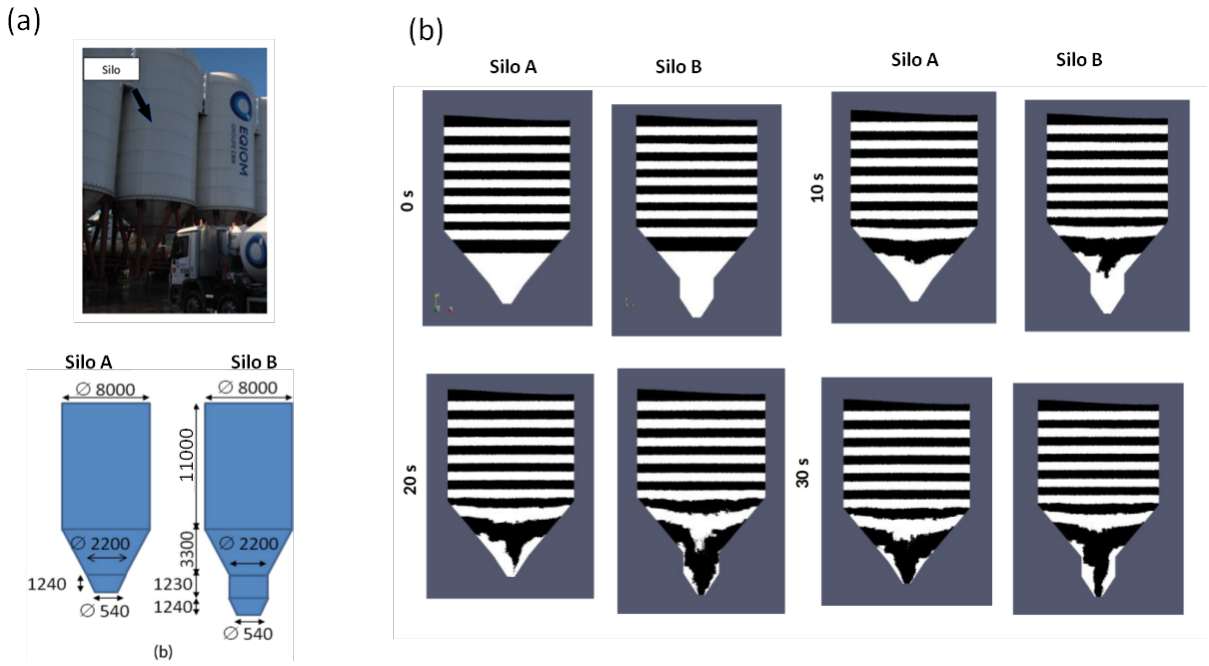

Figure 1. Hopper discharge for (a) Silo A; and (b) Silo B

Acknowledgements

The support of NVIDIA Corporation is gratefully acknowledged with the donation of the Titan X Pascal GPU used for this research. The exchanges with EQIOM Granulats and EQIOM Bétons concerning the concrete facility used in this study are greatly appreciated.

References

BlazeDEM3D-GPU, https://www.researchgate.net/project/Blaze-DEM-A-Large-Scale-GPU-Based-DEM-code

Duran J., 2012. Sands, powders, and grains: An introduction to the physics of granular materials. *Springer Science & Business Media*.

Cundall P.A. and Strack O.D.L, 1979. A discrete numerical model for granular assemblies. *Geotechnique,* 29, 47-65.

Govender N., Wilke D.N., Kok S. (2016), Blaze-DEMGPU: Modular high performance DEM framework for the GPU architecture. *SoftwareX,* 5, 62-66.

Govender N., Pizette P., Wilke D.N, Abriak N.E. (2015). Validation of the GPU based BLAZE-DEM frame-work for hopper discharge. *PARTICLES 2015, Barcelona*

Govender N., Wilke D.N., Pizette P., Abriak N-E,, 2018. A study of shape non-uniformity and poly- dispersity in hopper discharge of spherical and polyhedral particle systems using the BlazeDEM3D-GPU code. *Appl. Math. Comput*., 319, 318-336.

Pizette P, Govender N, Abriak N-E, Wilke D.N 2017. GPU DEM simulations and Experimental studies of ball milling process for various particle shapes. *Springer Proceedings Phys.*, 188, 1345–1352, DOI 10.1007/978-981-10-1926-5_141.

US Department of Energy, 2017. Mining Industry Bandwidth Study, *US Department of Energy BCS Incorporated*.

Wilke D.N, Govender N., Pizette P. and Abriak N-E. Computing with non-convex Polyhedra on the GPU. *Springer Proceedings Phys.,188*, 1371-1377, DOI 10.1007/978-981-0-1926-5_141